Performance of the Jet Energy Calibration at ATLAS using p_T Balance in Z + Jet Events

Pete Watson

Master of Science

Department of Physics

McGill University

Montreal, Quebec

February 7, 2011

A thesis submitted to McGill University in partial fulfillment of the requirements for the degree of Master of Science

©Peter G. F. Watson, 2010

DEDICATION

For Petey.

ACKNOWLEDGEMENTS

For those who helped me in the creation of this document, special thanks goes to my supervisor Dr. Brigitte Vachon, the postdocs Cibran Santamarina Rios and Malachi Schram, and all the members of the McGill ATLAS group. Extra thanks goes to Rodger Mantifel and Robert Keyes for providing me with important information and figures at the last minute. As well, thanks to Bertrand Chapleau for help in translating the abstract to French. Entertaining lunch breaks were made possible by Jason Schwartz, who needs to be mentioned. If it were not for the support of my wonderful wife Lorri, my family and my friends, I would have probably dropped out of graduate school long ago. To them I owe much thanks.

ABSTRACT

A precision measurement of the jet energy scale is essential for the success of the ATLAS experiment. This thesis investigates the suitability of p_T balancing in Z + Jet events as an *in situ* technique for assessing the performance of the jet energy calibration. While the technique is shown to have a kinematic bias in the region $p_T^Z < 60$ GeV/c, it is useful for studying jet performance at higher p_T^Z. The effects of background processes and signal selection criteria on the p_T balance are studied. This study also investigates the performance of jet reconstruction with various jet input constituents, jet algorithms and sizes, and jet calibration schemes.

ABRÉGÉ

Une mesure précise de l'échelle d'énergie des jets est indispensable pour la réussite de l'expérience ATLAS. La présente thèse examine la viabilité de l'équilibrage en p_T dans les événements Z + Jet en tant que technique *in situ* pour l'estimation de la performance de la calibration des jets. Bien que cette technique s'avère biaisée dans la région cinématique $p_T^Z < 60$ GeV/c, il est démontré qu'elle est utile dans un régime à haut p_T. Les effets des différentes contributions au bruit de fond ainsi que les critères de sélection du signal sur l'équilibrage en p_T sont étudiés. Cette étude examine aussi la performance de la reconstruction des jets avec différents constituants de jets, algorithmes et méthodes de calibration.

TABLE OF CONTENTS

LIST OF TABLES

LIST OF FIGURES

Figure page

CHAPTER 1
Introduction

The ATLAS (**A** **T**oroidal **L**HC **A**pparatu**S**) detector is a particle physics experiment at the Large Hadron Collider (LHC) at CERN, a particle physics laboratory near Geneva, Switzerland. The goal of ATLAS is to measure the fundamental properties of our universe by analysing the results of head-on collisions of protons at extraordinarily high energies.

1.1 Motivation

The most successful description of matter at its most fundamental level is a collection of quantum field theories known as the Standard Model. In this model, matter is represented by point-like spin 1/2 particles called fermions, which interact with each other via mediator spin 1 particles called bosons. Standard Model fermions are grouped into two categories, depending on the forces the particles experience: *Quarks*, which are subject to all forces (electromagnetic, weak and strong nuclear); and *Leptons*, which only interact through the electromagnetic and weak forces. A list of Standard Model fermions is shown in Table 1–1, along with their measured masses and electric charges. The quarks and leptons can be organised into three generations, which are identical to each other except for their masses, which increase from each generation. The origin of this structure is not fully understood and may be indicative of a theory more fundamental than the Standard Model.

Table 1–1: Standard Model fermions and their respective masses and electric charges [1].

Flavour	Mass [GeV/c^2]	Charge [e]
Leptons		
electron (e)	0.000511	-1
electron neutrino (ν_e)	$< 2 \times 10^{-9}$	0
muon (μ)	0.106	-1
muon neutrino (ν_μ)	$< 1.9 \times 10^{-4}$	0
tau (τ)	1.777	-1
tau neutrino (ν_τ)	$< 18.2 \times 10^{-3}$	0
Quarks		
up (u)	1.5 to 3.3$\times 10^{-3}$	+2/3
down (d)	3.5 to 6.0$\times 10^{-3}$	-1/3
charm (c)	1.27$\times 10^{-3}$	+2/3
strange (s)	70 to 130$\times 10^{-3}$	-1/3
top (t)	171.3$\pm$2.3	+2/3
bottom (b)	4.2	-1/3

Fermions interact with each other (or themselves) by exchanging a gauge boson. Table 1–2 lists the Standard Model bosons, along with the forces they mediate. The strong force is mediated by gluons, which carry a strong charge called "colour", analogous to electric charge. This interaction is described by an $SU(3)$ symmetry group called quantum chromodynamics (QCD), which means that there are three "colours" to the strong force (red, blue and green). The electromagnetic force is mediated by the photon, and the weak force is mediated by the W and Z bosons, which are both massive. The electromagnetic and weak forces can be unified and described by an $SU(2) \times U(1)$ symmetry group known as the electroweak interaction. This symmetry is thought to be broken spontaneously by the Higgs mechanism, which gives rise to the differing masses of the W, Z and massless photon. The Higgs mechanism requires the existence of the Higgs boson, a particle which has not yet been experimentally detected. An observation of the Higgs boson remains one of the final untested predictions of the Standard Model. Figure 1–1 summarises the interactions between Standard Model fermions and bosons.

Table 1–2: Standard Model gauge bosons and their respective masses and electric charges [1].

Name	Mass [GeV/c^2]	Charge [e]
Electroweak		
photon (γ)	$< 10^{-27}$	$< 10^{-35}$
$W^{\pm}$	80.4	±1
Z^0	91.2	0
Strong (colour)		
gluon (g)	0	0

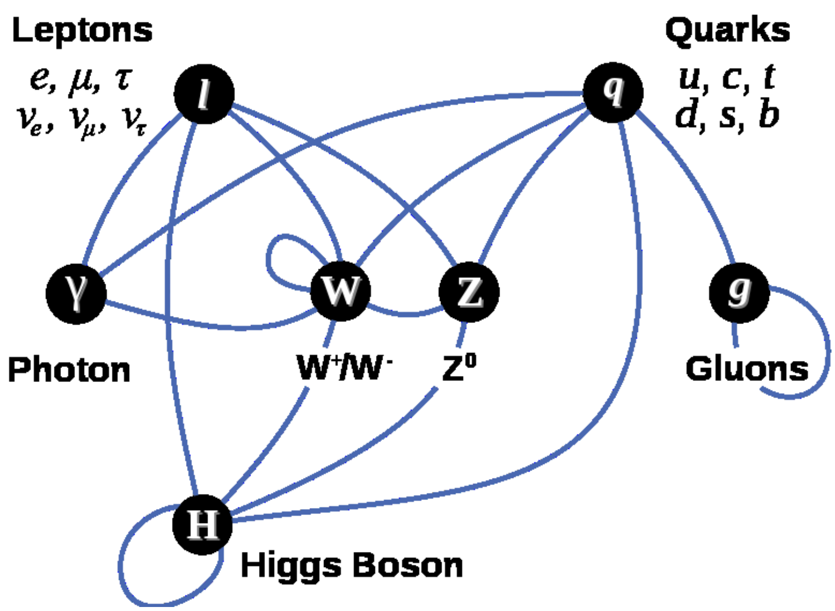

Figure 1–1: Standard model particles and their interactions [2].

While the Standard Model has been very successful in explaining observed particle properties to great precision, there is reason to suggest that it is not a complete theory and may be a subset of a more general theory. Some undesireable features of the Standard Model include the fact that it has 19 free parameters which must be input from experimental data, it can not explain the fermion generational structure, and it is unable to describe the gravitational interaction.

One approach for finding a complete theory of particle physics is to extend the Standard Model. Some common extentions include a new symmetry of nature, *supersymmetry*, which pairs each Standard Model fermion (boson) with a supersymmetric boson (fermion) partner. The most theoretically attractive supersymmetric models predict that these superparticles exist at the TeV scale and thus may be observed at the LHC [3].

ATLAS is often called a multi-purpose detector, in that it has been designed to be sensitive to as many interesting physics processes as possible. In addition to searching for the Higgs boson, supersymmetric particles and other new physics, ATLAS will also be able to make precision measurements of the Standard Model, including the mass of the top quark, CP-violation parameters, and the inclusive jet cross-section [3].

1.2 Description of LHC

The LHC is a proton-proton collider, installed in a 27 km long underground circular tunnel at CERN [4] (see Figure 1.2). The LHC is designed to accelerate two counter-rotating beams of protons to an energy of 7 TeV, or 99.9999991 percent the speed of light. At four separate interaction points, these two proton beams will collide with a center of mass energy of 14 TeV, an energy 7 times greater than is achievable at the Tevatron, the world's previously largest operational particle collider.

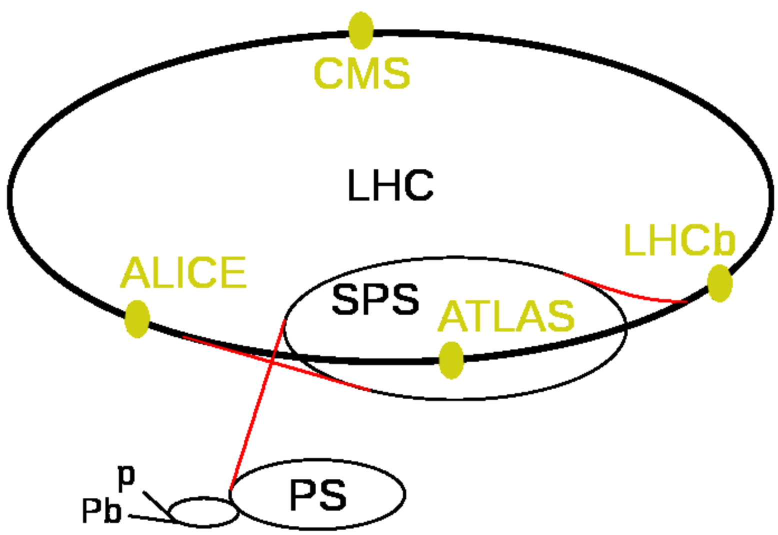

Figure 1–2: Diagram of the LHC accelerator chain and experiments. Protons (or lead ions) are accelerated and injected into the Proton Synchrotron (PS), which accelerates the particles to 26 GeV before entering the Super Proton Synchrotron (SPS), which further accelerates them to 450 GeV before final injection into the LHC. The four major detectors at the LHC (ATLAS, CMS, ALICE and LHCb) are also indicated.

The LHC also exceeds the Tevatron in instantaneous luminosity, which is a measurement of the rate of interactions per unit area. At full operation, the LHC is expected to have a luminosity of 10^{34} cm^{-2}s^{-1}. At this luminosity, bunches of protons will meet at the interaction points every 25 ns, with an average of 23 collisions taking place in each bunch crossing. This corresponds to over 900 million collisions per second. The number of recorded events of a particular process, N, is proportional to the integrated luminosity (instantaneous luminosity integrated over time) by:

$$N = \mathcal{L}\sigma\epsilon \tag{1.1}$$

where $\mathcal{L}$ is the integrated luminosity in units of inverse barns[1] , σ is the cross-section of the process in units of barns, and ϵ is the efficiency in identifying events from this process.

1.3 Description of ATLAS detector

In order to achieve the broad physics goals mentioned in Section 1.1, the ATLAS detector was designed with certain requirements [3]:

- Electronics and sensors must be able to handle radiation and high particle rate from LHC luminosity;
- Tracking of charged particles must be efficient and have good momentum resolution;
- Electromagnetic calorimetry must be able to identify photons and electrons efficiently, and hadronic calorimetry must be hermetic for accurate measurements of jets and missing transverse energy;
- Muon system must be self-contained and able to make high precision momentum measurements;
- Detector must have full azimuthal coverage and large pseudorapidity acceptance.

[1] 1 barn = 10^{-24} cm^2

The experiment makes use of a coordinate system defined with the origin at the center of the detector, which is the interaction point. The Z-axis is defined along the beam direction, the X-axis is along the horizontal with positive pointing towards the center of the LHC, and the Y-axis is along the vertical with positive pointing towards the sky. To describe features in the detector, certain quantities are used. The azimuthal angle ϕ is defined in the X-Y plane and is measured from the X-axis. A more useful quantity than the polar angle θ, measured from the Z-axis, is pseudorapidity, η, which is a Lorentz invariant along the Z-axis and defined as $\eta = -\ln(\tan(\theta/2))$. Lorentz invariant quantities are important in proton-proton collisions since the constituent quarks and gluons which collide frequently have a center-of-mass frame which is boosted in relation to the lab frame. A commonly used distance measurement in $\eta \times \phi$ space is $\Delta R = \sqrt{(\Delta\phi)^2 + (\Delta\eta)^2}$.

The detector is arranged into four main sub-detector systems, which are the Tracking System, the Calorimetry System, the Muon Spectrometer, and the Magnet System. The tracking system is situated at the center of the detector, and is comprised of the pixel detectors, the forward and barrel semiconductor trackers, and the transition radiation tracker. This system is used to identify and measure the momentum of charged particles. The calorimetry system is used to measure the energy of particles by completely absorbing them. It is divided into two types of calorimeters, electromagnetic and hadronic. The ATLAS calorimeters are covered in greater detail in Chapter 2. The muon spectrometer has the task of identifying and measuring the momentum of muons. It consists of monitored drift chambers, cathode strip chambers, resistive plate chambers and thin gap chambers. Muons are able to traverse the calorimeters without being stopped, so the muon spectrometer surrounds the calorimeters, as seen in Figure 1–3. The magnet system consists of the central solenoid and toroid magnets, both of which bend the trajectory of charged particles to measure their momenta.

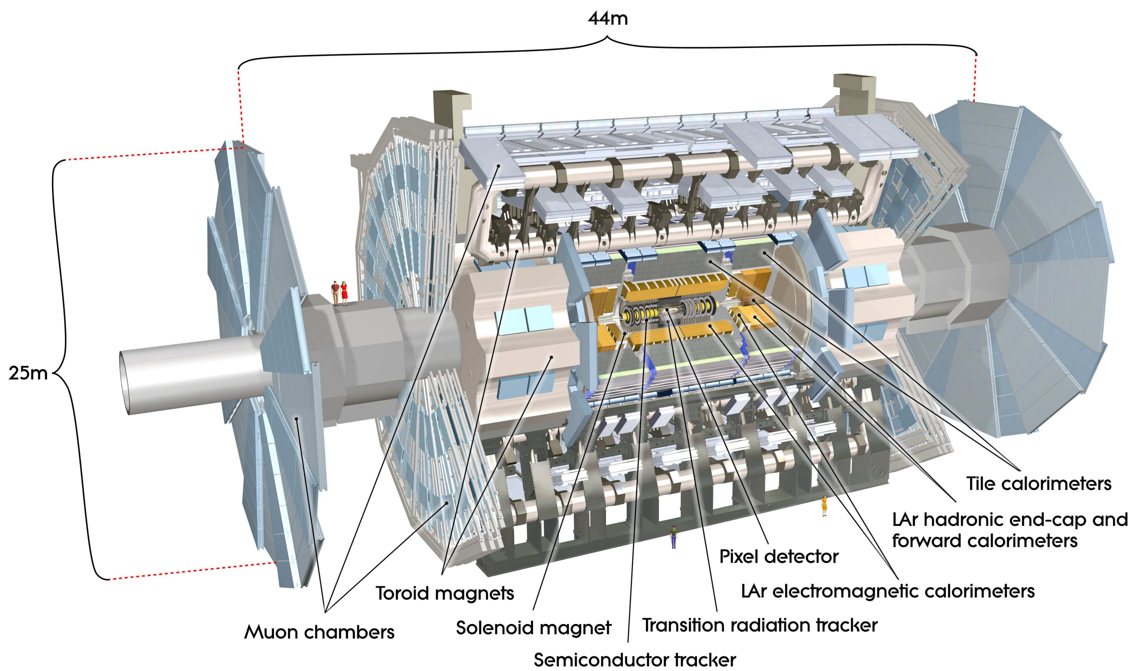

Figure 1–3: Schematic diagram of ATLAS detector and its sub-detectors.

One other important ATLAS system is the Trigger and Data Acquisition (TDAQ) system. Due to the immense rate of collisions in ATLAS ($\sim$ 1 billion per second), it is physically not possible to record every event using current technology. The TDAQ has the difficult task of reducing the rate of collisions to be recorded down to a manageable amount ($\sim$ 200 Hz), while not rejecting any "interesting" physics events. This complex chore is done using a three-level trigger system, comprised of both hardware and software based decision-making tools. To be recorded, an event must first meet the conditions of a *trigger signature*. These conditions are typically a combination of a physics object (i.e. an electron) and a threshold (i.e. $p_T \geq 25$ GeV/c). The ATLAS trigger system operates using numerous trigger signatures, in a list known as the trigger menu. To reduce the rates even further, some trigger signatures are *prescaled*, which means that of the events which meet the trigger signature conditions, only a fraction of them will be recorded.

CHAPTER 2
Calorimetry

In particle physics experiments, particles are detected by transfering some or all of their energy[1] to the detector medium by ionisation or excitation of the constituent atoms [5]. A calorimeter is a type of detector which measures the energy of a particle by completely absorbing it and converting its energy into an electrical signal. The mechanics of how it does this is covered in Section 2.1. Section 2.2 describes the calorimeters installed in ATLAS, and Section 2.3 discusses the issue of linearity and compensation in hadronic calorimetry. Chapter 3 brings all of these concepts together to explain how calorimeter signals are used to define and measure "jets".

2.1 Particle Interactions with Matter

From a calorimetry perspective, particle interactions with matter can be grouped into two broad categories: electromagnetic (EM) processes which mainly involve electrons, positrons and photons; and hadronic processes which deal with nuclear interactions between hadrons and matter.

[1] In the case of weakly interacting particles (neutrinos, new physics particles, etc.), they pass through the detector unscathed and do not deposit enough energy to be measured. This *missing energy* can be quantified and is an important signature in new physics searches.

2.1.1 Electromagnetic Showers

When an energetic electron, positron or photon interacts with matter, it initiates a cascade of secondary particles in what is known as an electromagnetic shower. This shower is caused by energy transfer from the incident particle to the medium through a variety of processes. The energy deposited by the shower in the calorimeter medium is measured, and from this the energy of the incident particle can be inferred.

The main processes by which photons interact with matter are the photoelectric effect, Compton scattering and pair production (which are covered extensively in [6]), however for energetic photons ($<$ 100 MeV), pair production is the dominant interaction. Pair production refers to the process where a photon with energy greater than $2m_ec^2$ interacts with the Coloumb field of a nucleus and then converts to an electron/positron pair, as shown in Figure 2–1.

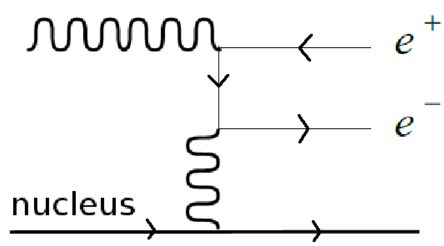

Figure 2–1: Feynman diagram of a photon undergoing pair production. The interaction with the nucleus is required to conserve momentum [7].

Energetic photons may also interact with an orbital electron in a process called triplet production, however this process has a smaller cross section than pair production[2] and can be ignored.

When a charged particle such as an electron or positron travels through matter, it transfers its energy mainly by the ionization and excitation of orbital electrons, and by radiating photons during interactions with nuclei (bremsstrahlung). At energies above the *critical energy* ($E_C \approx 550$ MeV/Z), bremsstrahlung is the dominant form of energy loss for electrons and positrons. Bremsstrahlung occurs much in the same way as pair production, in that the electron/positron interacts with the Coloumb field of a nucleus and is accelerated (i.e. deflected). The bremsstrahlung photon emitted by the accelerating charge is on average at an angle $\langle\theta_\gamma\rangle \propto m_e c^2/E$, with the electron/positron trajectory, thus at high energies, bremsstrahlung radiation forms a collimated cone around the electron/positron.

From these dominant processes, the development of an electromagnetic shower can be modelled. In one such simple model (Rossi-Heitler [8]), an incoming energetic electron can radiate a hard bremsstrahlung photon, which can then undergo pair production to create an electron and positron, which can then radiate photons, and so on. This process may continue until the energy of the charged particles drops below E_C, at which point the shower reaches a maximum. After this point, photons begin to deposit their energy by Compton scattering or photoelectric effect,

[2] For photon energies greater than 100 MeV, $\sigma_{pair}/\sigma_{triplet} \approx Z$, where Z is the atomic mass of the medium.

and the remaining electrons/positrons undergo ionization processes until they are absorbed (or annihilated) by the medium. Figure 2–2 shows the development of an electromagnetic shower using the Rossi-Heitler model.

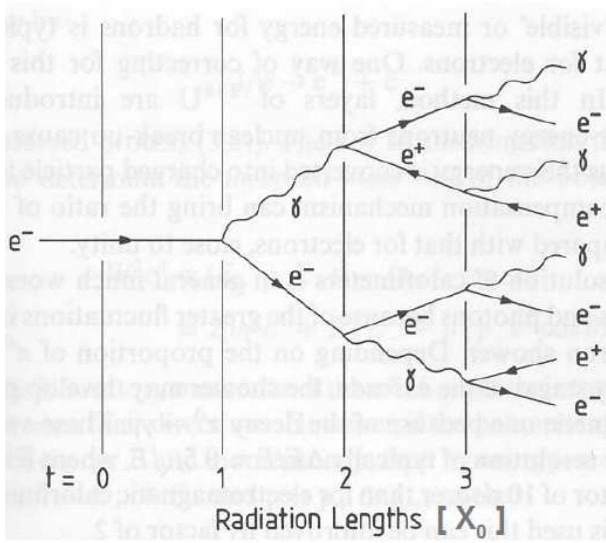

Figure 2–2: Diagram of an electromagnetic shower using the Rossi-Heitler model. Radiation length X_0 is defined as the thickness of material required to reduce the average electron energy by a factor e ($\sim 63\%$) [8].

2.1.2 Hadronic Showers

In addition to electromagnetic interactions, hadrons are also able to interact with matter through the strong force. This leads to complex nuclear interactions where many other types of secondary particles are produced, with large event-by-event fluctuations. This in turn means that hadronic showers also exhibit large statistical fluctuations due to the large number of possible interactions available to hadrons.

When a high energy hadron interacts with matter, it typically strikes a nucleus and causes spallation. This produces a number of nuclear fragments and secondary hadrons which can then interact with other nuclei, or disintegrate into other particles (see Figure 2–3). Similar to an EM shower, a hadronic shower will develop until the hadrons do not have enough energy to break up nuclei. After this point, hadrons will mainly lose energy through ionization or will be absorbed in a nuclear process. The multiplicity of particles in a hadronic shower grows logarithmically with the incident hadron energy.

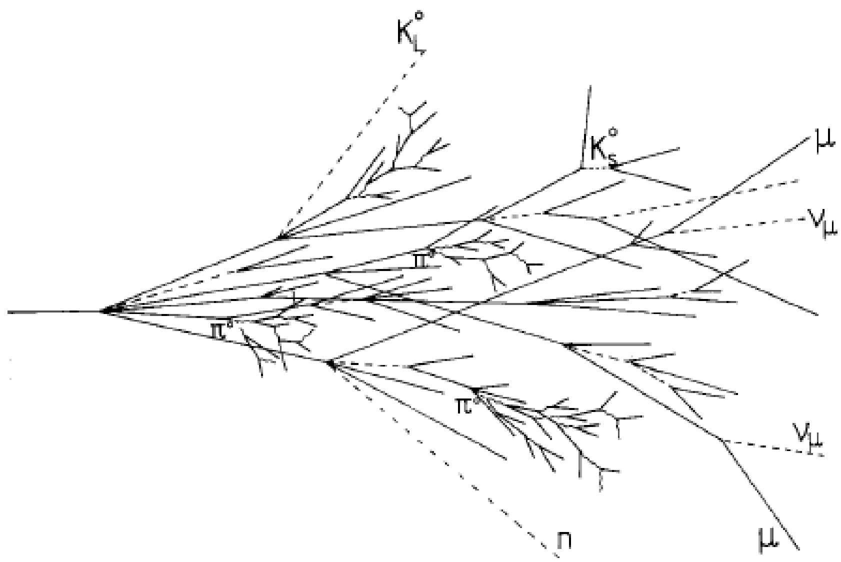

Figure 2–3: Diagram of a typical hadronic shower [7].

Due to the nature of nuclear interactions, the mean free path for an interaction (also called nuclear interaction length λ_I) is much larger than the electromagnetic radiation length X_0 for a given material. This means that a hadronic shower must travel further longitudinally in a material to deposit all of its energy than an electromagnetic shower. Experimentally, because of the long longitudinal development of hadronic showers, hadronic calorimeters are often made of a dense material and are installed "downstream" from electromagnetic calorimeters.

2.2 ATLAS Calorimeters

The ATLAS calorimeter system consists of five subsystems, each covering a particular pseudorapidity region: the electromagnetic barrel and electromagnetic end-cap cover $|\eta| < 3.2$, the hadronic tile calorimeter covers $|\eta| < 1.7$, the hadronic end-cap covers $1.5 < |\eta| < 3.2$, and the forward calorimeters cover $3.1 < |\eta| < 4.9$. The individual ATLAS calorimeter subsystems can be seen in Figure 2–4. All of the calorimeters in ATLAS are *sampling calorimeters*, which are a class of calorimeters which use a passive medium to develop electromagnetic and hadronic showers (usually made of high Z material), sandwiched with an active medium which measures the energy deposited by the showers. The calorimeter subsystems can be classified in terms of their sampling technology, namely those that use liquid argon or scintillating plastic as the active material.

2.2.1 Liquid Argon Calorimeters

Liquid argon sampling calorimeters are the most common type of calorimeter technology employed in ATLAS. They function by measuring the peak ionization current produced by charged particles from electromagnetic and hadronic showers which pass through and ionize the liquid argon. The peak ionization current is proportional to the incident energy of the charged particles.

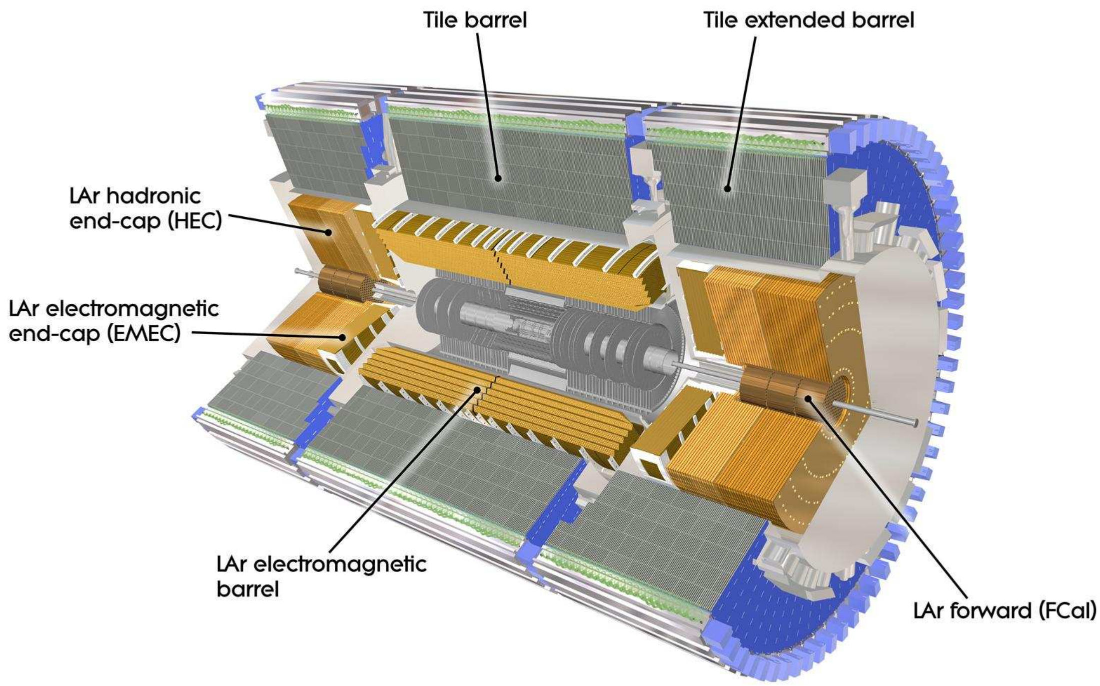

Figure 2–4: Schematic diagram of the ATLAS calorimeter system.

The electromagnetic barrel and end-cap calorimeters use thin lead sheets to initiate shower development, with narrow gaps of liquid argon in between. The lead sheets are arranged in an accordion structure to provide full ϕ coverage and fast signal extraction (see Figure 2–5). There is a crack in the region where the electromagnetic barrel and electromagnetic end-cap meet ($1.3 < |\eta| < 1.6$) which has very poor energy resolution. The hadronic end-cap calorimeter is also a liquid argon sampling calorimeter, but uses copper plates arranged in wheels as its passive medium.

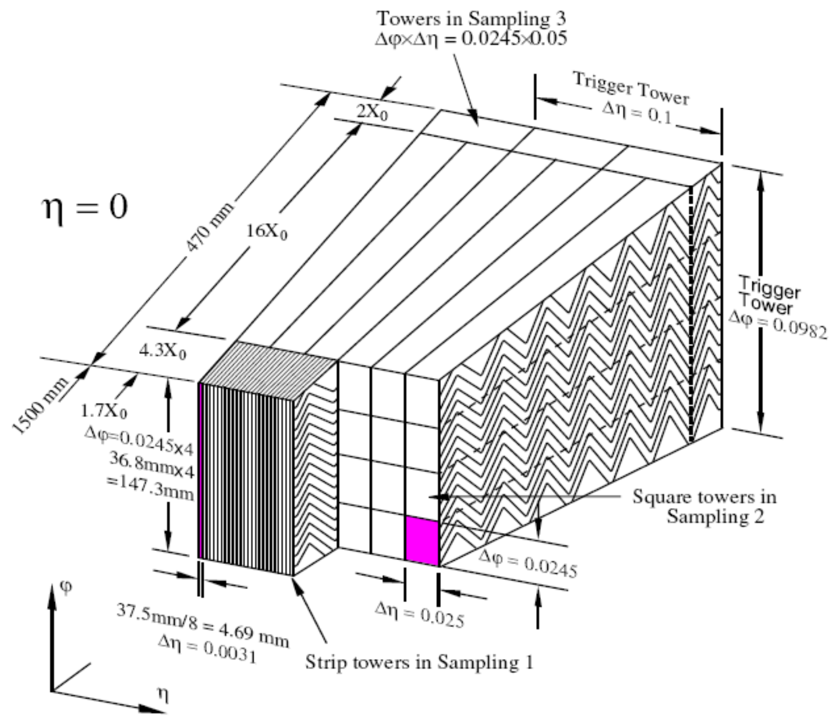

Figure 2–5: Sketch of a module of the electromagnetic barrel calorimeter. This figure shows its accordion structure, as well as its granularity and longitudinal segmentation.

2.2.2 Scintillating Tile Calorimeters

The hadronic tile calorimeter uses steel as an absorber and plastic scintillator as the active medium, which produces UV light when ionizing particles pass through it. The orientation of the scintillating tiles is radial and normal to the beam axis, as shown in Figure 2–6, which allows for near total ϕ coverage. The hadronic tile calorimeter is shielded by the electromagnetic barrel calorimeter and the solenoid magnet of the inner detector, providing a large amount of extra material to contain hadronic showers. The main function of the hadronic tile calorimeter is to make a good measurement of electromagnetic and hadronic shower energies which penetrate the electromagnetic calorimeters, and to improve the resolution of the missing energy measurement.

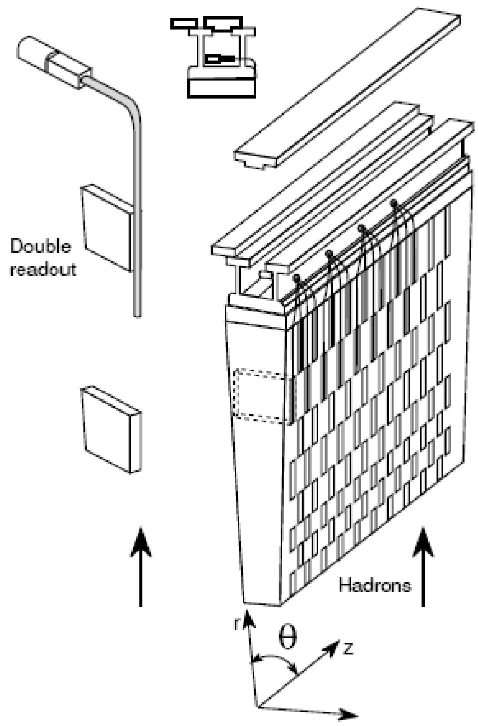

Figure 2–6: Sketch of a tile from the hadronic tile calorimeter and its orientation in ATLAS. The large amount of longitudinal segmentation allows for a good measurement of hadronic shower depth.

2.3 Compensation and Linearity

In a hadronic shower, energy will be transfered to the medium via electromagnetic (ionization, $\pi^0 \rightarrow \gamma\gamma$, etc.) and hadronic (fission, nuclear binding energy, neutron elastic scattering, etc.) interactions. In the hadronic component, energy transfered to nuclear binding, nuclear excitation and slow neutrons is fundamentally undetectable by the calorimeter. As well, hadronic production of neutrinos and muons which escape the detector leads to undetected energy. The fraction of energy deposited by electromagnetic and hadronic processes in a hadronic shower is energy dependent and varies widely from event to event.

The ratio between the efficiency in measuring energy deposited via electromagnetic and hadronic interactions is given by e/h, where e is the electromagnetic response and h is the hadronic response of the calorimeter[3] . In general, most calorimeters have $e/h > 1$, since not all hadronic energy is sampled. It is possible to construct a *compensating* calorimeter which increases h and decreases e such that $e/h = 1$. This is often done by using a fissionable material (e.g. ^{238}U) as the passive medium, which helps to recover the missing energy from slow neutrons. In the case of ATLAS, it is also possible to have a non-compensating calorimeter and use offline software techniques to tune $e/h = 1$.

Compensation is a desirable feature as it improves the resolution and linearity of the calorimeter. The energy resolution of a calorimeter, $\sigma(E)$, is a function of e/h [9]:

$$\frac{\sigma(E)}{E} \propto \frac{k_1}{\sqrt{E}} + k_2 \cdot |e/h - 1| \tag{2.1}$$

[3] Response is defined as $E_{measured}/E_{true}$

with $k_i > 0$. The e/h term comes from event-by-event fluctuations in the fraction of electromagnetic energy in hadronic showers. Thus, for a compensated calorimeter this term disappears leading to an improvement in resolution.

The linearity of a calorimeter refers to its response being independent of energy. One can write the response of a calorimeter to hadronic showers ($R_{\pi^\pm}$) as:

$$R_{\pi^\pm} = f_{EM} \cdot e + f_h \cdot h \tag{2.2}$$

$$= f_{EM} \cdot e + (1 - f_{EM})h \tag{2.3}$$

$$= (e - h)f_{EM} + h \tag{2.4}$$

where f_{EM} and f_h refer to the energy dependent fraction of EM and hadronic energy deposited by the shower, with $f_{EM} + f_h = 1$. Thus, for a compensated calorimeter the non-linear f_{EM} term vanishes [10].

2.4 Electromagnetic Energy Scale

The energy deposited by a particle interacting with the ATLAS calorimeter system is first effectively measured as a collection of electronic signals. A combination of detailed Monte Carlo simulation studies and test beam analysis is necessary to translate these signals into a meaningful measurement of energy. In a test beam, a portion of the calorimeter is placed directly in the path of a particle (electron, pion, photon, muon or proton) beam with known energy. By comparing the measured calorimeter signal to the energy of the incident particle beam, the calorimeter response can be measured and a calibration can be applied. The ATLAS calorimeters have been tuned using electron and muon beams such that $e = 1$. Because of this, the ATLAS calorimeters are said to be tuned to the "electromagnetic energy scale" [11].

By construction, the ATLAS calorimeters are non-compensating, which means their response to hadronic interactions is not the same as their response to electromagnetic interactions ($e/h > 1$). To properly account for the energy deposited by hadrons in the calorimeters, corrections must be applied using software. The calculation of energy corrections for hadronic showers in a non-compensating calorimeter is an involved procedure, and is covered in more detail in Section 3.3.1.

CHAPTER 3
Jets

Many physics analyses at ATLAS search for events with jets and/or missing tranverse energy at the detector level. In most of these analyses the reconstruction of jet energy is the leading source of systematic uncertainty, and in some cases they require the so-called jet energy scale to be known to within 1% [3]. A precise measurement of the jet energy scale is then crucial for these analyses.

3.1 Jet Production

As mentioned in Section 1.1, the strong force affects particles carrying a colour charge (quarks and gluons), much like how the electromagnetic force is experienced by particles with an electric charge. For colour to be conserved in strong interactions, quarks must carry one of the three possible colours, while gluons must carry two, one colour and one anticolour. Both experimental data and theory suggest that colour is confined, which means that quarks and gluons cannot appear in isolation and must exist as colour-neutral combinations called *hadrons*. The two observed colourless combinations are classified as *baryons*, which have three differing colours or anticolours and *mesons*, which have one colour and its anticolour.

After a hard collision at the LHC, a recoiling parton (quark or gluon) will *fragment*, that is as it moves away from other coloured particles, it becomes energetically favourable to create a quark-antiquark pair from the vacuum. This scenario is analogous to stretching a magnetic dipole; rather than isolating a magnetic monopole, it becomes energetically favourable for a new dipole to be created [12]. This process produces a shower of quarks and gluons, which then recombine as hadrons in what is called *hadronisation*. Since the original recoiling parton has momentum, the products of hadronisation appear as a spray of particles collimated in the same direction as the initial parton, in what is called a *jet*. Figure 3–1 displays the evolution of a jet, from a parton to a particle jet which eventually interacts with the ATLAS detector.

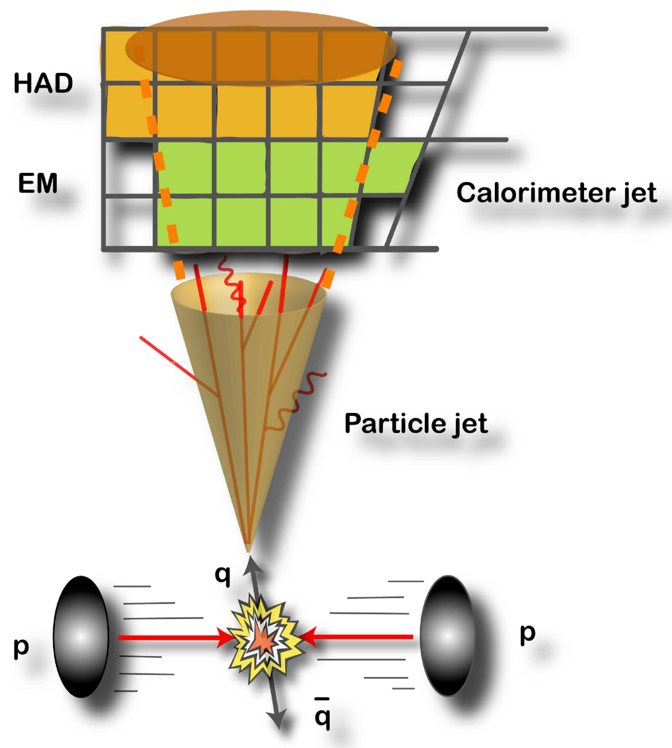

Figure 3–1: Diagram showing the evolution of jet formation. A parton from the hard process radiates and hadronises to create a particle jet, which deposits energy in the calorimeters. Signals from the calorimeter are used to reconstruct a calorimeter jet.

3.2 ATLAS Jet Reconstruction

In an experiment like ATLAS, it is impossible to tell which particles measured by the detector came from which initial parton. As such, jets are identified by applying a clustering algorithm on signals from the calorimeter. The goal of the algorithm is to construct jets which have kinematic properties (i.e. direction and momenta) related to the properties of the initial parton [13]. Jet algorithms used in ATLAS fall into two groups, *cone algorithms* which group particle objects together within a specific radius in $\eta \times \phi$ space, and *sequential recombination algorithms* which recursively cluster particles together within some distance in momentum and geometrical space.

3.2.1 Jet Algorithms

The most common jet finders used in ATLAS are seeded fixed-cone algorithms and sequential recombination algorithms [11]. The seeded fixed-cone jet finder takes as input calorimeter objects and orders them in decreasing transverse momentum p_T. If the highest p_T object, or seed, is above the seed threshold (> 1 GeV), all objects within a user-defined radius of ΔR from the seed are combined, and a direction is calculated from their combined four-momenta. A new cone is placed around this direction, and the objects inside it are again recombined. This procedure continues until the direction of the cone does not change, at which point it is considered stable and is saved as a jet. The algorithm then builds a cone around the second highest p_T object from the seed list, and continues until no more seeds are available. If some cone jets overlap, a split-merge algorithm quantifies this overlap fraction and merges the jets if the amount is greater than some threshold[1] . A narrow ($\Delta R = 0.4$) and wide ($\Delta R = 0.7$) cone jet algorithm exist as defaults in ATLAS.

An example of a sequential recombination jet finder in ATLAS is the k_T algorithm [11]. This jet finder calculates the distance d_{ij} between pairs of calorimeter objects, defined as:

$$d_{ij} = \min(p_{T,i}^2, p_{T,j}^2)\frac{\Delta R_{ij}^2}{D^2} \tag{3.1}$$

where D is a parameter of the algorithm, typically set to 0.4 or 0.6. The algorithm also calculates $d_i = p_{T,i}^2$ for each object. Next, the minimum of all d_i and d_{ij} is found and labelled $d_{\min}$. If $d_{\min}$ is a d_{ij}, objects i and j are merged. If $d_{\min}$ is a d_i, object i is saved as a jet. These steps proceed until all objets have been identified or merged as jets. Unlike cone algorithms, no objects are shared between jets in the k_T algorithm. A related jet finder is the anti-k_T algorithm [14], which follows the same steps but calculates the distance variables as:

$$d_{ij} = \min(p_{T,i}^{-2}, p_{T,j}^{-2})\frac{\Delta R_{ij}^2}{D^2} \tag{3.2}$$

$$d_i = p_{T,i}^{-2}. \tag{3.3}$$

Because the anti-k_T algorithm calculates the minimum p_T^{-2} difference between input objects rather than p_T^2, it tends to combine soft particles with hard particles, rather than clustering soft particles together. This leads to the advantageous feature that anti-k_T jet shapes in $\eta \times \phi$ are sensitive to hard radiation, but change very little with

[1] ATLAS default is > 0.5

the addition of soft radiation. Due in part to this feature of jet shape resilience, the anti-k_T algorithm is the default ATLAS jet algorithm.

3.2.2 Jet Inputs

For a jet algorithm to be executed, it requires a list of input objects which it may cluster. Ideally, these objects would be the final state particles from an interaction. In simulation data, this information is available and jets built from these particles are known as "truth jets". For real collisions, the signals these particles make in the calorimeters are used as input. ATLAS uses two principle calorimeter signal object definitions, *projective towers* and *topological clusters*.

Projective towers are calorimeter cells in an $\eta \times \phi$ window of 0.1×0.1, which projects outward from the interaction point. The ATLAS calorimetry system has a total of 6400 towers. Tower energy can be negative due to electronic noise fluctuations, so to ensure the jet input has positive energy, negative towers are merged with neighboring positive towers to obtain a net positive object.

Topological clusters (or TopoClusters) are three-dimensional clusters of calorimeter cells, which represent the shower produced by an incoming particle interacting with the detector. Cells are grouped together using a nearest-neighbor algorithm, which suppresses noise by construction. A seed cell is defined by a signal-to-noise ratio[2] above a threshold S. All neighboring cells are grouped as a cluster around the seed cell. Next-to-nearest neighbor cells are added to the cluster if they are above a threshold N. Next-to-next-to-nearest neighbor "guard" cells are added to the cluster

[2] In other words, $|E_{\mathrm{cell}}| > S\sigma_{\mathrm{noise}}$.

if they are above a threshold P. The ATLAS default is S=4, N=2, P=0 [11]. Once this clustering procedure has been applied, the cluster is analysed for local maxima. If more than one maximum is found, the cluster is split between the maxima.

These two concepts can be combined to produce another calorimeter signal object, the *topological tower* or (TopoTower). Topological towers are built by first creating topological clusters. A projective tower is then made by selecting calorimeter cells from topological clusters contained in a 0.1×0.1 area of $\eta \times \phi$. Since topological towers are composed of cells from topological clusters, they are also noise-suppressed [15]. Figure 3–2 illustrates the geometric configuration of projective towers, topological clusters and topological towers.

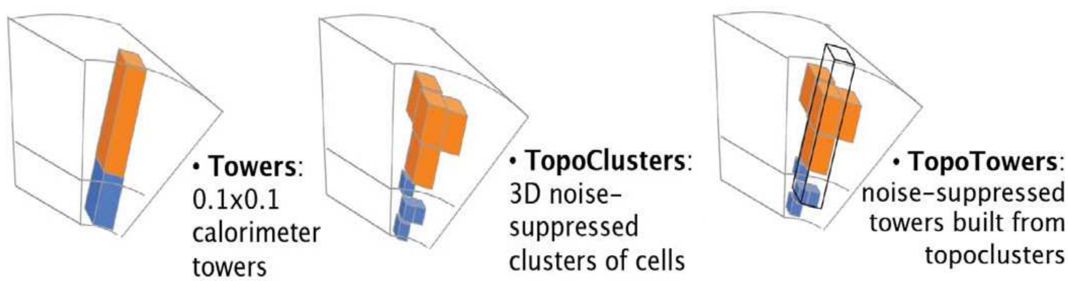

Figure 3–2: Illustration of ATLAS calorimeter jet input objects. In this diagram, the calorimeter volume segments represent an area in $\eta \times \phi$, projected outward from the ATLAS interaction point. The blue and orange cells (in lower and upper segments) refer to the electromagnetic and hadronic calorimeters, respectively [16].

3.3 Jet Energy Scale

The jet energy scale (JES) is the relationship between the energy of a jet reconstructed from calorimeter signals to the energy of the initial parton which fragmented and created the jet. A related quantity, the jet energy resolution (JER), gives the possible variation of the reconstructed jet energy (related to Equation (2.1)). Knowledge of the jet energy scale and jet energy resolution is therefore integral to the analysis of both signal and background events involving final state partons. In addition to these analyses, the jet energy scale also has an impact on the measurement of missing transverse energy, which is a key signature for many new physics searches at the LHC. A poor understanding of the jet energy scale would lead to an under or over estimation of missing transverse energy.

As mentioned in Section 2.3, since jets contain hadrons, a portion of their energy will not be detected due to the non-compensation of the ATLAS calorimeter system. In addition to non-compensation, the jet energy scale also has contributions from other calorimeter effects, such as electronic noise, non-instrumented (dead) material, and cracks between calorimeter subsystems.

On top of calorimeter effects, the jet energy scale is also affected by physics processes. This is due to a limitation of jet algorithms; they are not able to infallibly distinguish the calorimeter signals left by particles coming from the fragmentation of a particular parton. As such, a reconstructed jet will not typically include all of the energy from the initial parton due to radiation that escaped the jet algorithm (out-of-cone radiation). There will also be energy included in the reconstructed jet which originated from a source other than the initial parton (the underlying event and pile-up[3]).

3.3.1 Jet Energy Calibration

The process of setting the jet energy scale at ATLAS involves applying a series of software corrections to the energy of a reconstructed jet, and is known as the jet energy calibration. There are two principle jet energy calibration schemes used at ATLAS: *cell energy density weighting* and *local hadronic* calibration. Both of these schemes are based on the idea that electromagnetic showers have a higher energy density and smaller physical shape than hadronic showers[4] . One major difference between these two schemes is that cell energy density weighting applies a calibration *after* jets have been reconstructed, while the local hadronic calibration scheme calibrates the calorimeter signal objects *before* jet algorithms are executed.

Cell energy density weighting is a technique which was borrowed from the H1 experiment [17], and jets calibrated using this scheme are typically referred to as "H1 calibrated". The basic idea behind this approach is that hadronic showers will most often leave a lower energy density in calorimeter cells compared to electromagnetic showers. These low density cells are compensated by applying a signal weight of the

[3] The underlying event refers to all event activity excluding the hard scattered partons. Pile-up refers to additional proton collisions in each bunch crossing, as well as signals from previous bunch crossings.

[4] This is related to the electromagnetic radiation length X_0 being smaller than the nuclear interaction length λ_I.

order e/π. The technique begins with jets which have been reconstructed from uncalibrated (EM scale) towers or topological clusters. All calorimeter cells contributing to a jet are given a weighting factor based on their energy density and location in the ATLAS detector. The weighting factors are derived from Monte Carlo simulated events and range from ≈ 1 for high density cells, to 1.5 for low density cells.

The local hadronic calibration [18] scheme begins with uncalibrated topological clusters. Based on the shape and energy of the cluster, it is classified as either "electromagnetic-like" or "hadronic-like"[5] . The calorimeter cells of hadronic-like clusters are weighted in a style similar to the cell energy density weighting technique. Once this has been done, both electromagnetic-like and hadronic-like clusters are corrected for other calorimeter effects, such as energy deposits in the calorimeter but outside of calorimeter clusters (Out-of-cluster corrections), and energy deposits in material outside of the calorimeters (dead material corrections).

In addition to the cell energy density weighting and local hadronic calibration schemes, ATLAS also employs another method of correcting the jet energy scale, known as *global re-scaling*. Global re-scaling is a simple p_T and η dependent correction factor which when applied, brings the jet response[6] to 1, on average. The re-scale factors have been calculated from Monte Carlo simulation samples, using

[5] The classification is derived from GEANT4 [19] simulations of charged and neutral pion interactions.

[6] Jet response is defined as $\frac{E_{jet}^{calib}}{E_{jet}^{truth}}$, where E_{jet}^{calib} is the calibrated jet energy and E_{jet}^{truth} is the truth jet energy.

the so-called numerical inversion technique [20]. The global re-scaling method has the ability to be applied on both uncalibrated (electromagnetic scale) and calibrated (cell energy density weighting and local hadronic) jets.

CHAPTER 4
Z + Jet p_T Balance Technique

The ATLAS calibration schemes for establishing the jet energy scale rely heavily on Monte Carlo simulation, both for modelling the production of jets and the response of the calorimeters. It is important that the performance of these calibrations be cross-checked using real data *in situ* to better understand the jet energy scale. This thesis investigates an *in situ* technique for measuring the performance of the jet energy calibration: Z + Jet p_T balancing.

4.1 *In situ* Test of JES

In the presence of real data, the jet energy calibration must be validated *in situ* using suitable physics processes. A physics process is deemed suitable if it yields sufficient statistics with good background discrimination. This section will give a cursory overview of *in situ* calibration strategies at ATLAS; for a full treatment of the subject, see [11].

One common *in situ* technique is p_T balancing. To first order, the sum of all transverse momenta in an event[1] at ATLAS should be zero. A non-zero sum of p_T in an event from a process containing jets could indicate a flaw with the jet energy calibration. Using the p_T balancing technique with different types of physics

[1] Taking into account missing energy.

processes allows for various aspects of the jet energy calibration to be studied. The p_T balance in events where two energetic partons are produced (Dijet events) can be used to study how uniform the calibration is with respect to η and ϕ. Dijet events are also useful for measuring the jet energy resolution. The p_T balance in events where a parton is produced in association with a γ or Z boson[2] provides a measure of the absolute jet energy scale by comparing the hadronic energy of a jet with an object which deposits its energy electromagnetically (γ, $e^{\pm}$, $\mu^{\pm}$). Since the ATLAS calorimeters are tuned to the electromagnetic scale, the energy of these objects will be measured accurately[3] . All of the *in situ* processes listed have been used to validate the jet energy scale in previous collider experiments, including the Collider Detector at Fermilab (CDF) [21].

4.2 Production of Z + Jet Events

This study will focus on the p_T balance of Z + Jet events. At leading order, Z + Jet events are produced by the processes shown in Figure 4–1. The cross section at LHC energy (7 TeV) for these events, where the Z decays to e^+e^- or $\mu^+\mu^-$, is on the order of $\sim$ 150 pb. This corresponds to approximately 150 000 events in the first run of data taking at the LHC[4] . The expected cross section for Z($\rightarrow e^+e^-$) + Jet events compared to other physics processes of interest is shown in Figure 4–2.

[2] Where the Z decays to e^+e^- or $\mu^+\mu^-$.

[3] The energy of $\mu^{\pm}$ is measured using tracking information from the inner detector and muon spectrometer.

[4] Assuming an integrated luminosity of $\mathcal{L} = 1$ fb^{-1}.

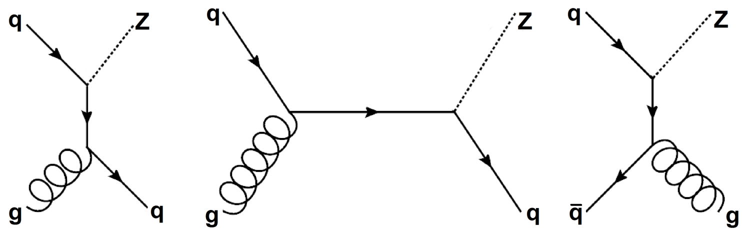

Figure 4–1: Leading order Feynman diagrams for Z + Jet production in proton-proton collisions. The direction of time is from left to right.

The production of γ + Jet events follows similar processes as Z + Jet, with the Z in Figure 4–1 replaced by a γ. Because of their similarities, the p_T balance of these two types of physics processes provide a set of complimentary *in situ* tests of the jet energy calibration. An advantage to using the γ + Jet process is that its cross section is $\sim$ 100 times larger than that of Z + Jet. This is due to the larger center-of-mass energy required to produce a Z compared to the massless photon, as well as suppression from requiring the Z to decay leptonically. However, the contamination from processes which "fake" a γ + Jet event is expected to be $\sim$ 100 larger than that for Z + Jet events [23, 24].

A feature of Z + Jet events is that by looking at both $Z(\rightarrow e^+e^-)$ and $Z(\rightarrow \mu^+\mu^-)$ decay channels, the reconstructed reference value of p_T^Z can be cross checked between the electron and muon channels. This is a useful systematic check, as the properties of reconstructed electrons and muons are measured using different detector subsystems, namely the electromagnetic calorimeter and muon spectrometer.

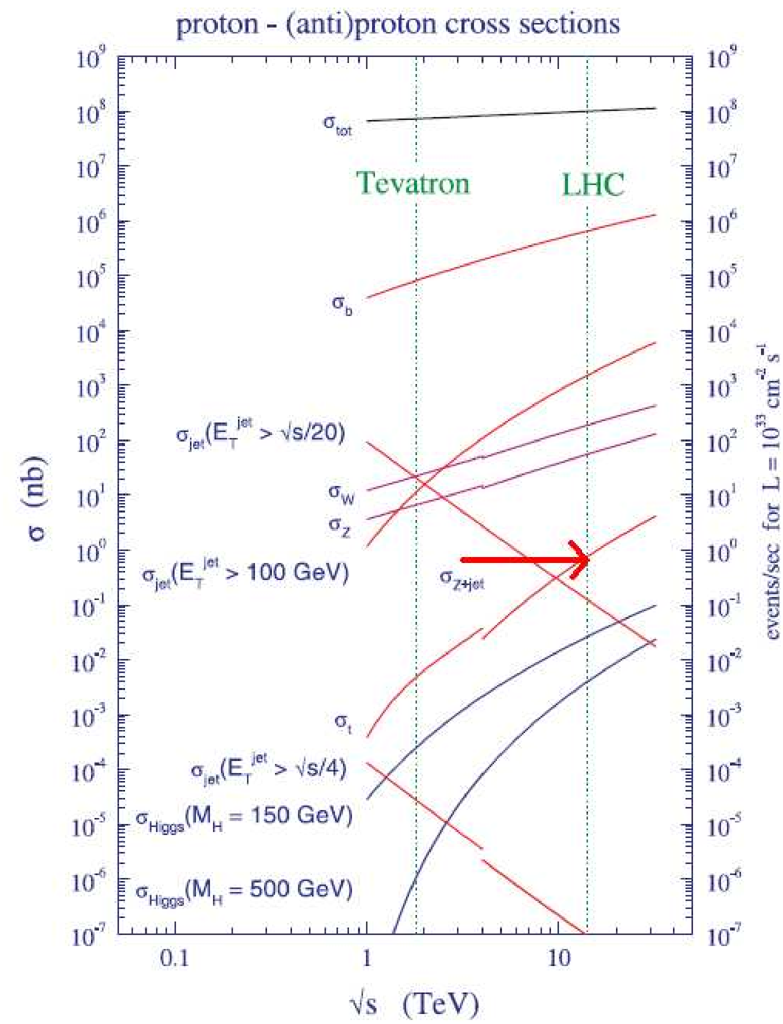

Figure 4–2: Expected cross sections for various physics processes at LHC energy [22]. The expected cross section for Z($\rightarrow e^+e^-$) + Jet events is indicated by an arrow.

4.3 Kinematics of p_T Balancing

In the center-of-momentum frame (COM) of γ/Z + Jet events, conservation of momentum in the transverse plane leads to the equation:

$$\vec{p}_T^{\,\gamma/Z} + \vec{p}_T^{\,parton} = 0 \tag{4.1}$$

where the momentum of the γ or Z boson exactly balances the momentum of the parton. In reality, due to initial state radiation (ISR) and the primordial transverse momentum (k_T) of the partons within the colliding protons [25], the center-of-momentum frame and the lab frame are not invariant in the transverse plane. When transforming to the lab frame, Equation (4.1) becomes

$$\vec{p}_T^{\,\gamma/Z} + \vec{p}_T^{\,parton} + \vec{p}_T^{\,initial} = 0 \tag{4.2}$$

where $\vec{p}_T^{\,initial}$ is the contribution from ISR and primordial k_T. This initial transverse momentum upsets the perfect balance between the momentum of the γ/Z and parton from the so-called "hard process", as visualised by Figure 4–3.

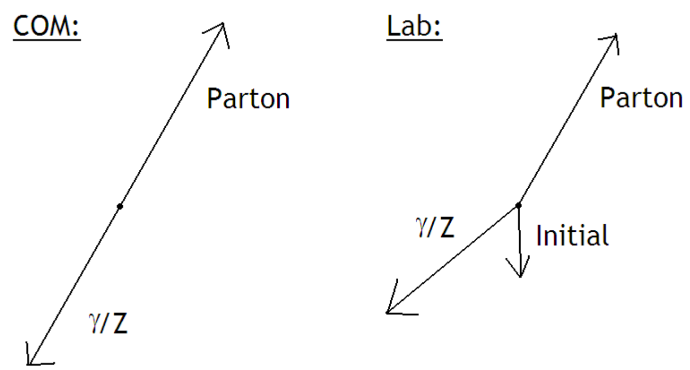

Figure 4–3: A schematic representation of p_T balance in COM and lab frame.

This momentum imbalance in Z + Jet events can be better understood when considering the kinematics of two-body ($2 \rightarrow 2$) reactions (see Figure 4–4). In the center-of-momentum frame, the energies (E_Z, E_{parton}) and momenta (p_Z, p_{parton}) of the outgoing particles are:

$$E_Z = \frac{s + m_Z^2 - m_{parton}^2}{2\sqrt{s}}, \quad E_{parton} = \frac{s + m_{parton}^2 - m_Z^2}{2\sqrt{s}} \tag{4.3}$$

$$p_Z = \pm\sqrt{E_Z^2 - m_Z^2}, \quad p_{parton} = \mp\sqrt{E_{parton}^2 - m_{parton}^2} \tag{4.4}$$

where s is the Mandelstam variable defined by $s = (p_1 + p_2)^2$, and p_1, p_2 are the incoming parton momenta. For all Standard Model partons (excluding the top quark), we can make the assumption that $m_Z^2 >> m_{parton}^2$. This simplifies Equations (4.3) and (4.4) to

$$E_Z = \frac{s + m_Z^2}{2\sqrt{s}}, \quad E_{parton} = \frac{s - m_Z^2}{2\sqrt{s}} \tag{4.5}$$

$$p_Z = \pm\frac{s - m_Z^2}{2\sqrt{s}}, \quad p_{parton} = \mp\frac{s - m_Z^2}{2\sqrt{s}}. \tag{4.6}$$

In this form, it is evident that the Z and parton both have equal and opposite

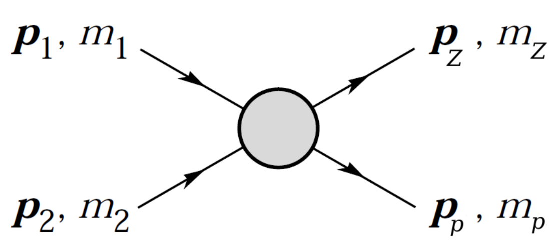

Figure 4–4: Diagram of a 2 → 2 reaction.

momenta, however due to the mass of the Z, an asymmetry exists between their energies.

To transform from the center-of-momentum frame to the lab frame, the energies and momenta of the outgoing particles must be boosted. This is done by a Lorentz transformation in the direction of the relative motion between the lab and COM frames, $\vec{u}$. For a COM frame moving with a relative velocity $\beta = v/c$ to the lab frame, the energy and momentum in the lab frame (E^*, p^*) are given by [1]

$$\begin{pmatrix} \gamma & -\gamma\beta \\ -\gamma\beta & \gamma \end{pmatrix} \begin{pmatrix} E \\ p_\parallel \end{pmatrix} = \begin{pmatrix} E^* \\ p_\parallel^* \end{pmatrix}, \quad p_T = p_T^* \tag{4.7}$$

where $p_\parallel$ and p_T are the momentum components parallel and perpendicular to the direction of the boost, and $\gamma = (1-\beta^2)^{-1/2}$. It is important to note that because the direction of the boost is not necessarily along the beam axis, the transverse plane in the COM is not necessarily the same as in the lab.

Using the COM energies and momenta previously derived for the Z and parton, in the lab frame they take the form

$$\begin{pmatrix} E^* \\ p_\parallel^* \end{pmatrix} = \begin{pmatrix} \gamma\frac{s\pm m_Z^2}{2\sqrt{s}} \mp \gamma\beta\frac{s-m_Z^2}{2\sqrt{s}}\vec{u}_\parallel \\ -\gamma\beta\frac{s\pm m_Z^2}{2\sqrt{s}} \pm \frac{s-m_Z^2}{2\sqrt{s}}\vec{u}_\parallel \end{pmatrix} \tag{4.8}$$

where $\vec{u}_\parallel$ refers to the projection of the particle momentum on to the direction of the boost. Here, the energy asymmetry between the Z and parton observed in the COM frame has been transformed into an energy and *momentum* asymmetry in the lab frame. From Equation (4.8), it is not immediately clear what is the size of the effect the momentum difference between the Z and parton will have on the p_T balance. To study this further, a simplified "toy" Monte Carlo program was created to simulate these events.

4.3.1 Toy Monte Carlo

Using Equation (4.8), the momenta distributions of the outgoing Z and parton can be calculated for toy collisions at the LHC. Events are simulated by providing a momentum distribution for the incoming partons (p_1 and p_2), calculating the momenta and energies of the outgoing Z and parton in the COM frame, then boosting the Z and parton back to the lab frame. Once in the lab frame, useful quantities such as the p_T balance can be calculated. In this study, the p_T balance was defined as $p_T^{parton}/p_T^Z - 1$, and the initial p_T of the interaction as $|\vec{p_T^1} + \vec{p_T^2}|$.

The magnitudes of $\vec{p_1}$ and $\vec{p_2}$ were randomly generated following a Landau distribution with a most probable value of 40 GeV/c and sigma of 10 GeV/c. This distribution and these values were chosen as a reasonable approximation for the incoming parton momentum spectrum at the LHC. The directions of $\vec{p_1}$ and $\vec{p_2}$ were set by generating values for ϕ and α, where ϕ is the usual azimuthal angle and α is the polar angle measured from the beam axis (see Figure 4–5). Since the direction of the incoming partons should be ϕ independent, ϕ was randomly generated between 0 and 2π. To control the amount of initial p_T, α was randomly sampled following a gaussian distribution with a mean, $\langle\alpha\rangle$, left as a free parameter. As the mean $\langle\alpha\rangle$ increased, the average initial p_T of the interaction increased (see Figure 4–6a). Thus $\langle\alpha\rangle$ can be thought of as a measure of the average initial p_T.

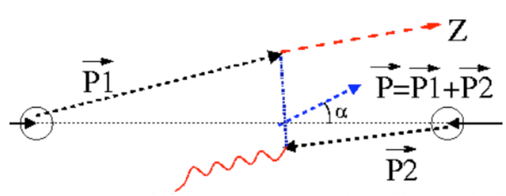

Figure 4–5: Definition of variable α used in toy Monte Carlo code.

The effect of initial p_T of the interaction on the p_T balance is evident in Figure 4–6b. For increasing values of $\langle\alpha\rangle$, the width of the p_T balance distribution also increases. This is not surprising, as Equation (4.2) indicates that for sufficient values of initial p_T, the probability for having an unbalanced event ($p_T^{parton}/p_T^Z - 1 \neq 0$) increases, smearing the distribution.

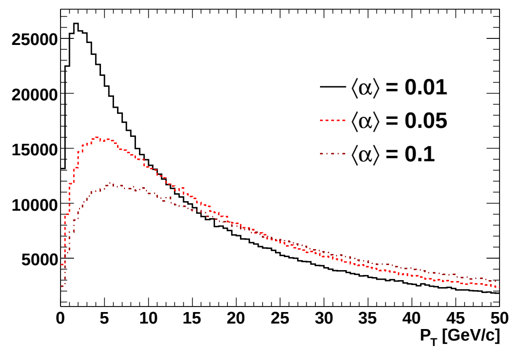

(a) Initial p_T of interaction

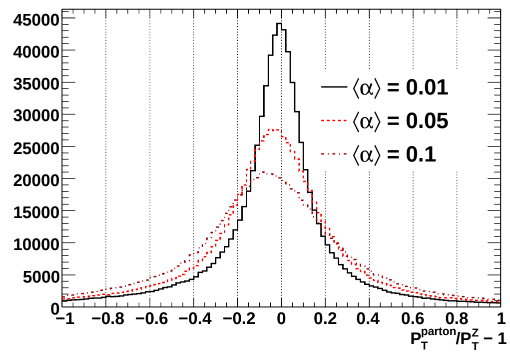

(b) p_T Balance

Figure 4–6: Distribution of initial p_T (a) and p_T balance (b) for several $\langle\alpha\rangle$ values (in radians).

A more interesting effect is the shift of the mean of the p_T balance distribution for increasing values of $\langle\alpha\rangle$, which is not apparent from Equation (4.2). As the amount of average initial p_T increases, the mean of the p_T balance distribution shifts to a negative value, implying $\langle\frac{p_T^{parton}}{p_T^Z}\rangle < 1$. This trend suggests that on average, the initial momentum (and its transverse projection) of the interaction is not shared equally between the outgoing Z and parton, leading to a p_T imbalance. This momentum imbalance can be understood kinematically from Equation (4.8).

4.3.2 Limitations of Toy Monte Carlo

A toy monte carlo is precisely that, a simplified "toy" model used to understand a more complicated process. This simplification leads to limitations in the model's accuracy in describing nature. The toy Monte Carlo used in this study is no exception, and some of its short comings are listed here.

In the toy simulation, the momentum distributions of the incoming partons ($\vec{p_1}$ and $\vec{p_2}$) were determined using the same input Landau function, yet were uncorrelated. In reality, there is a strong correlation between the momentum of the two partons which produce a Z + Jet event, as witnessed in Figure 4–7.

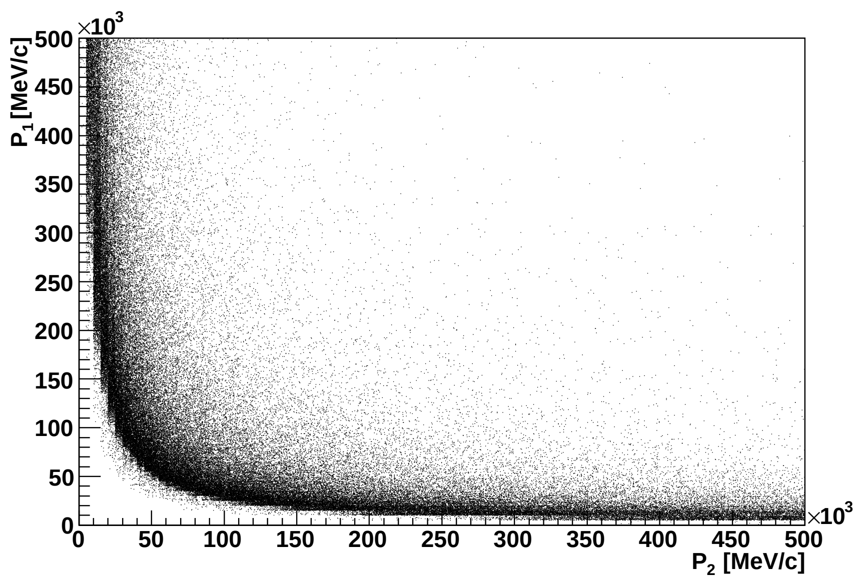

Figure 4–7: Plot of p_1 versus p_2 in Z + Jet events simulated with PYTHIA [26]. Correlation between the momentum of the two incoming partons is evident.

This plot indicates that for Z + jet production, it is probable that a less energetic incoming parton (i.e. $p < 50$ GeV/c) will interact with a highly energetic parton ($p > 50$ GeV/c), leading to a boosted final state.

Another inaccuracy of the toy Monte Carlo is how α is parton energy independent. It is expected that at the LHC, an incoming parton will have $\alpha \approx 0$. Large values of α are only expected if the parton undergoes ISR, effectively boosting it in the transverse plane. By conservation of energy, after ISR the parton would have a lower energy than before. Thus one would expect that incoming partons with large α would have an average energy less than partons with small α. The toy Monte Carlo does not include this effect.

Despite the limitations of the toy Monte Carlo, it is still useful for studying the kinematics of Z + Jet events. In particular, it suggests a potential effect from initial p_T of the interaction on the p_T balance, which should not be greatly influenced by the model's simplifications.

4.4 p_T Balance Definition

Aside from initial p_T, there is an other factor which contributes to the shape of the p_T balance distribution: the chosen definition of p_T balance. For one, the balance definition of:

$$B = \frac{p_T^{jet}}{p_T^Z} - 1 \tag{4.9}$$

is asymmetric by construction; it has a minimum at -1 and a maximum at ∞. An alternative balance definition of:

$$A = \frac{2(p_T^{jet} - p_T^Z)}{p_T^{jet} + p_T^Z} \tag{4.10}$$

is more symmetric, with a minimum and maximum of -2 and 2, respectively. This definition, however, is slightly more complex than Equation (4.9)and from a measurement of A, it is not as straightforward in determining the relationship between p_T^Z and p_T^{jet} as a measurement of B.

Looking at the definitions given by Equations (4.9) and (4.10), an asymmetry in the p_T balance distributions could be attributed to event-by-event fluctuations if the variance of the denominator is greater than the variance of the numerator. To study this, a set of toy p_T^Z and p_T^{jet} distributions were generated following random Gaussian distributions, both with a fixed mean of 20 GeV/c. The width of the p_T distributions, $\sigma(p_T)$, was left as a free parameter. By varying the width of the p_T^Z and p_T^{jet} distributions, and calculating the event-by-event p_T balance, the effect of fluctuations on the p_T balance distribution shape for the two balance definitions can be tested.

Figure 4–8 shows the p_T balance distributions for (a) Equation (4.9) and (b) Equation (4.10), with $\sigma(p_T^Z) = 5$ GeV/c and $\sigma(p_T^{jet}) = 2.5$ GeV/c. As can be seen, the distribution given from Equation (4.9) is more asymmetric than the distribution given from Equation (4.10). Also, the peak of the Equation (4.9) distribution is shifted more from 0 than the Equation (4.10) distribution.

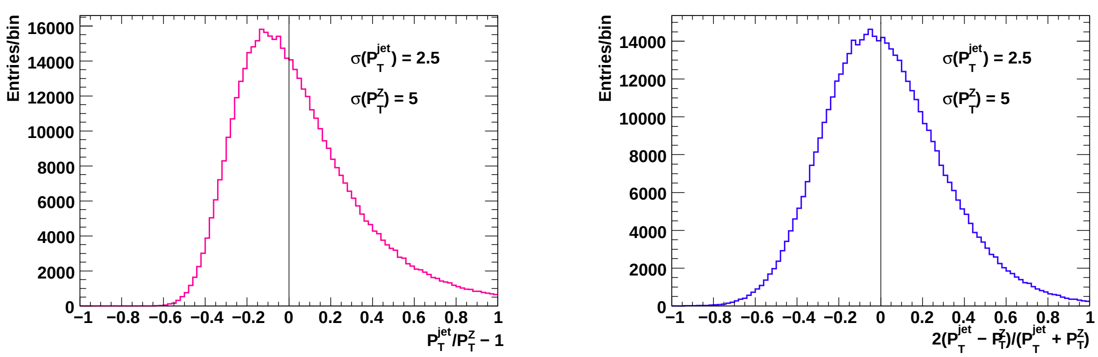

(a) $B = \frac{p_T^{jet}}{p_T^Z} - 1$

(b) $A = \frac{2(p_T^{jet} - p_T^Z)}{p_T^{jet} + p_T^Z}$

Figure 4–8: Comparison of p_T balance distributions for the definitions (a) Equation (4.9) and (b) Equation (4.10), in the case where $\sigma(p_T^Z) > \sigma(p_T^{jet})$.

If the situation is reversed and $\sigma(p_T^Z) < \sigma(p_T^{jet})$, the shapes of the p_T balance distributions change. Figure 4–9 shows the p_T balance distributions for the two definitions, only with $\sigma(p_T^Z) = 2.5$ GeV/c and $\sigma(p_T^{jet}) = 5$ GeV/c. In this case, the distribution given by Equation (4.9) is more symmetric than the distribution given by Equation (4.10), and its peak is closer to 0. Based on these trends, the p_T balance definition of Equation (4.9) is best suited for the case where $\sigma(p_T^Z) < \sigma(p_T^{jet})$. The p_T resolution of electrons and muons used to reconstruct the momentum of the Z boson is expected to be smaller than the p_T resolution of jets at ATLAS for values less than $\sim$ 200 GeV/c [11]. After reconstruction, the p_T resolution of the Z boson is still expected to be smaller than that for jets in this momentum region. For the remainder of this analysis, the p_T balance definition of Equation (4.9) will be used.

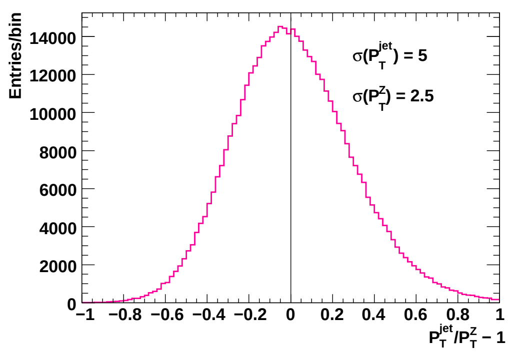

(a) $B = \frac{p_T^{jet}}{p_T^Z} - 1$

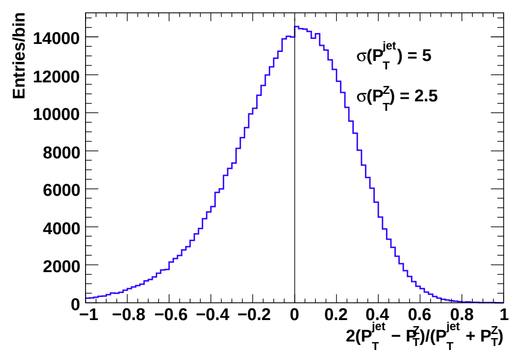

(b) $A = \frac{2(p_T^{jet} - p_T^Z)}{p_T^{jet} + p_T^Z}$

Figure 4–9: Comparison of p_T balance distributions for the definitions (a) Equation (4.9) and (b) Equation (4.10), in the case where $\sigma(p_T^Z) < \sigma(p_T^{jet})$.

CHAPTER 5
Z + Jet p_T Balance Study

The previous chapter used a simple toy Monte Carlo simulation to investigate the p_T balancing technique in Z + Jet events, and highlighted the effects of the initial p_T of the interaction and the choice of p_T balance definition. In this chapter, the study will be performed on official ATLAS simulation datasets, at both the parton and reconstructed level. The effect of background processes and signal selection criteria will also be investigated.

5.1 Monte Carlo Simulated Datasets

This study was performed on standard ATLAS Monte Carlo samples generated at $\sqrt{s} = 7$ TeV and $\sqrt{s} = 10$ TeV, as listed in Tables 5–1, 5–2 and 5–3. The 7 TeV signal samples were generated using ALPGEN [27], which is a leading order matrix element generator for hadronic collisions. To model parton showering, ISR and hadronisation, ALPGEN is interfaced with another event generator, called HERWIG [28]. Within HERWIG, the effects of the underlying event are modelled with software known as JIMMY [29]. Because ALPGEN calculates leading order matrix elements, the events generated for this study have exactly one outgoing parton, which fragments and hadronises into a jet. Jets produced from parton showering in HERWIG are then matched with the matrix element jet using the MLM matching scheme [30] to avoid double counting jets.

Table 5–1: 7 TeV Monte Carlo simulated datasets used for $Z \rightarrow e^+e^-+$ Jet and $Z \rightarrow \mu^+\mu^-+$ Jet signal.

Process	$\hat{p}_T$ range	Cross section	# of Events
$Z \rightarrow e^+e^-+$ 1 parton	$>$ 15 GeV/c	1.34×10^2 pb	63K
$Z \rightarrow \mu^+\mu^-+$ 1 parton	$>$ 15 GeV/c	1.34×10^2 pb	63K

The 10 TeV signal and background processes[1] were generated using PYTHIA 6.4, a general-purpose high energy collider simulation optimised for $2 \rightarrow 2$ processes. PYTHIA uses leading order matrix elements to model the hard process of interest (i.e $pp \rightarrow Z+$ Jet), and includes the effects of parton showering, ISR, underlying event, hadronisation, and unstable particle decay. To generate more events in the kinematic region of interest, most samples are produced with a minimum (or maximum) $\hat{p}_T$ threshold[2] .

The particle four-vectors generated from ALPGEN and PYTHIA are interfaced with GEANT4, which simulates their interaction with the material and magnetic field of the ATLAS detector and any further decays of unstable particles. Interactions which occur in an instrumented "active" portion of the detector are classified as hit-objects. The next step in the ATLAS Monte Carlo sample generation is to simulate the response of the detector from all hit-objects, in a procedure called digitisation. The final information stored after digitsation (electronic signals from the ATLAS detector) is identical in form to the digitisation information that would be recorded

[1] The $t\bar{t}$ sample hard process was generated using AcerMC [31] and interfaced with PYTHIA, which handled ISR, hadronisation and decays.

[2] $\hat{p}_T$ is the p_T of the outgoing parton(s) in a $2 \rightarrow 2$ process, in the COM frame.

Table 5–2: 10 TeV Monte Carlo simulated datasets used for $Z \rightarrow e^+e^-+$ Jet signal and backgrounds.

Process	$\hat{p}_T$ range	Cross section	# of Events
$Z \rightarrow e^+e^-+$ Jet	$>$ 10 GeV/c	6.12×10^2 pb	198K
QCD(dijet)	8-17 GeV/c	1.17×10^{10} pb	397K
QCD(dijet)	17-35 GeV/c	8.67×10^8 pb	394K
QCD(dijet)	35-70 GeV/c	5.60×10^7 pb	198K
QCD(dijet)	70-140 GeV/c	3.28×10^6 pb	142K
QCD(dijet)	140-280 GeV/c	1.52×10^5 pb	150K
QCD(dijet)	280-560 GeV/c	5.12×10^3 pb	296K
QCD(dijet)	560-1120 GeV/c	1.12×10^2 pb	219K
$t\bar{t} \rightarrow l + X$	-	1.07×10^2 pb	98K

Table 5–3: 10 TeV Monte Carlo datasets used for $Z \rightarrow \mu^+\mu^-+$ Jet signal and backgrounds. In the QCD($b\bar{b} \rightarrow \mu\mu + X$) sample, the $\hat{p}_T$ range refers to the leading and second leading p_T muon, respectively.

Process	$\hat{P}_T$ range	Cross section	# of Events
$Z \rightarrow \mu^+\mu^-+$ Jet	$>$ 10 GeV/c	6.12×10^2 pb	194K
$t\bar{t} \rightarrow l + X$	-	1.07×10^2 pb	98K
QCD($b\bar{b} \rightarrow \mu\mu + X$)	$> 6, > 4$ GeV/c	6.54×10^4 pb	873K
$W \rightarrow \mu\nu+$ Jet	$>$ 10 GeV/c	5.94×10^3 pb	172K

with real proton collisions. The final stage in producing an ATLAS dataset is known as reconstruction. During reconstruction, the information from digitisation is run though various pattern-recognition algorithms, which try to identify physics objects (photons, electrons, jets, etc.), along with their energy and direction.

5.2 Z + Jet p_T Balance - Leading Jet Method

As mentioned in Section 4.3, due to higher order physics effects, the p_T of the Z boson will not always be equal in magnitude to that of its associated parton. This can be seen in Figure 5–1, where Z + Jet events are spread over the diagonal (where $p_T^{parton} = p_T^Z$) as a result of the initial p_T of the interaction.

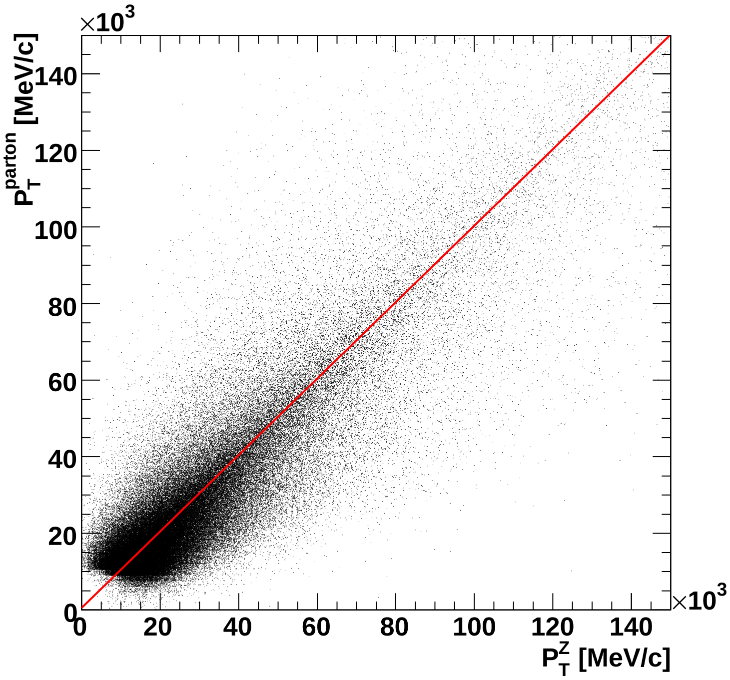

Figure 5–1: p_T of the parton versus p_T of the Z in simulated Z + Jet events, generated with $\hat{p}_T > 10$ GeV. The diagonal red line indicates where $p_T^{parton} = p_T^Z$.

In general, the Z boson p_T should equal the sum of transverse momenta of *all* the jets in the event, if more than one jet is produced. In light of this, the definition of p_T balance could be

$$B_\Sigma = \frac{|\Sigma_{jets}\vec{p_T}|}{p_T^Z} - 1. \tag{5.1}$$

However, for the purposes of testing the calibration of a single jet, it is more straightforward to define the p_T balance as in Equation (4.9), where p_T^{jet} is the p_T of the highest transverse momentum jet of the event (leading jet), which is assumed to have originated from the parton associated with the Z. For this definition to be a meaningful measure of jet energy calibration performance, events must be selected carefully to avoid effects which would disturb the balance.

5.2.1 Analysis Algorithm

For this study, the p_T balance is calculated according to the following procedure:

1. For each event, a signal jet and Z are retrieved, based on defined selection criteria. If the jet or Z do not meet the selection criteria, the event is rejected.
2. The balance, B, of the event is computed and binned in both a kinematic (p_T^Z or p_T^{avg})[3] and spatial (η^{jet} or ϕ^{jet}) variable. This binning allows for the jet calibration to be studied either as a function of momentum, or position in the ATLAS detector.
3. In each kinematic and spatial bin, the bin-average balance is quantified by fitting a Gaussian function to the balance distribution. This is done by an

[3] In this study, $p_T^{avg} = \frac{1}{2}(p_T^Z + p_T^{jet})$.

iterative fitting procedure, where first a Gaussian fit is applied in a range of ± 1 RMS from the distribution histogram mean. The mean (μ) and sigma (σ) of the fitted Gaussian are extracted, and another Gaussian fit is applied to the balance distribution in a range of $\pm\sigma$ from μ. The fitted mean is considered "stable" if the variation of μ from consecutive fits is less than 1%. If no stable mean is found after 3 fits, the balance distribution histogram is rebinned, reducing the total number of bins by a factor of 2. The described fitting procedure is then repeated, again with a maximum of 3 fits. If no stable mean is found by this point, the balance distribution is considered to not have a well-defined peak, and the kinematic or spatial bin is not used in the analysis.

4. The stable mean from each kinematic and spatial bin, as well as the fitted error on the mean, is plotted against the kinematic or spatial variable.

5.3 p_T Balance - Parton Level

The p_T balance technique was first explored at the parton level. This was done by looking at the 10 TeV Z + Jet simulation data and identifying the incoming partons (after ISR) of the $2 \rightarrow 2$ interaction, and the outgoing Z and parton. The initial p_T of the interaction was calculated as the transverse component of the sum of momentum of the two incoming partons.

The shape of the p_T balance distribution for all simulated Z + Jet events is shown in Figure 5–2a. The distribution is asymmetric with a non-Gaussian tail, and its peak is slightly shifted from an expected balance of 0. For Z + Jet p_T balancing to be a viable *in situ* technique, the balance distribution at the parton level should be as symmetric as possible with minimal tails and should have a peak at perfect balance ($p_T^{parton}/p_T^Z - 1 = 0$). From the arguments in Chapter 4, the distorted shape of the distribution is most likely caused by the initial p_T of the interaction.

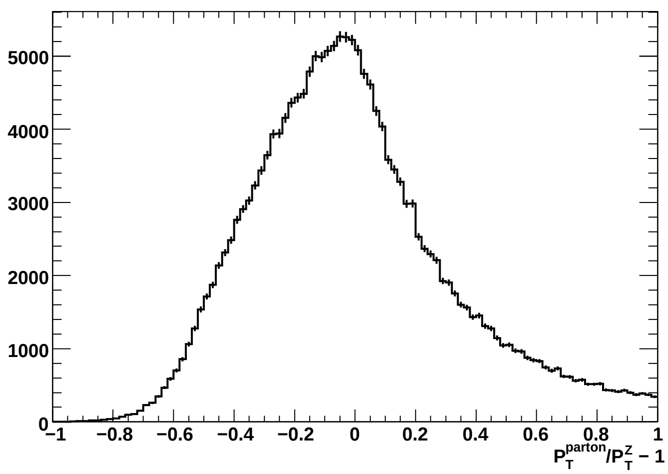

(a) All Z + Jet events

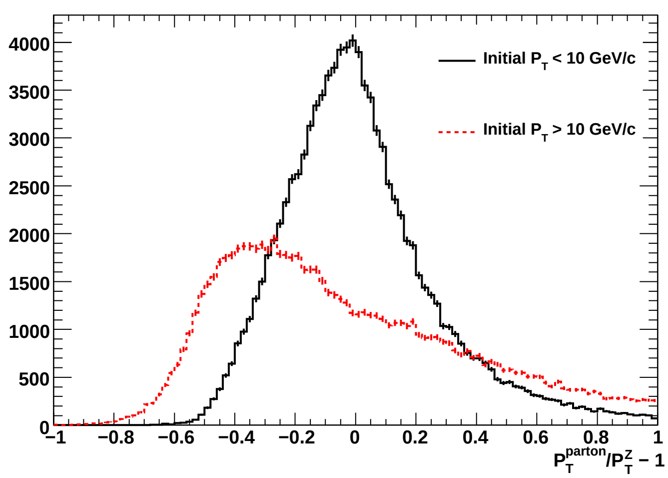

(b) All Z + Jet events in bins of initial p_T

Figure 5–2: p_T balance distributions of simulated Z + Jet events at parton level. The asymmetry and tail of the distribution (a) is mainly due to events produced with significant initial p_T (b). The Y axis of (a) and (b) has units of simulated events per bin.

To investigate the influence of initial p_T on the balance distribution, events were histogrammed according to the magnitude of initial p_T for that interaction. As can be seen in Figure 5–2b, events produced with large ($>$ 10 GeV/c) initial p_T form a major contribution to the tail and asymmetry of the distribution. In simulation data, these events can be excluded from the Z + Jet p_T balance sample by explicit calculation of initial p_T. However, in real data this is not feasible, thus another quantity must be used to discriminate events with large initial p_T.

One indication of substantial initial p_T in a Z + Jet event comes from the event topology. In the plane transverse to the beam direction, the outgoing Z and parton should be "back-to-back", that is $|\phi^Z - \phi^{parton}| = \pi$. Any initial p_T which is not aligned with the Z or parton will disturb this quantity, leading to $|\phi^Z - \phi^{parton}| < \pi$ (see Figure 4–3). Defining $\Delta\phi = |\phi^Z - \phi^{parton}|$, events can be selected by requiring a minimum value for $\Delta\phi$. Figure 5–3 shows the correlation between $\Delta\phi$ and the initial p_T of the interaction, with most low initial p_T events clustered near $\Delta\phi \approx \pi$. The effect of applying a $\Delta\phi$ cut on the balance distribution is seen in Figure 5–4. Setting the minimum $\Delta\phi$ requirement to be closer to π results in a more symmetric distribution, but also reduces the amount of available statistics.

The shape of the balance distribution is also influenced by the generator $\hat{p_T}$ threshold, which intrinsically biases the simulation data. By imposing a minimum p_T requirement for the Z and parton which is larger than the $\hat{p_T}$ threshold, as well as a cut on $\Delta\phi$, the balance distribution becomes much more symmetric and the tail is reduced (see Figure 5–4). Recognising this low p_T bias, the analysis presented

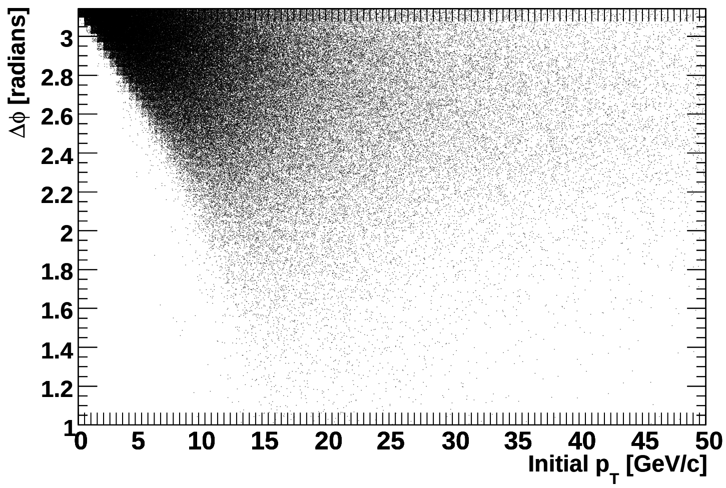

Figure 5–3: Correlation between $\Delta\phi$ and the initial p_T of the interaction in simulated Z + Jet events. Events with low initial p_T tend to be "back-to-back", with $\Delta\phi \approx \pi$.

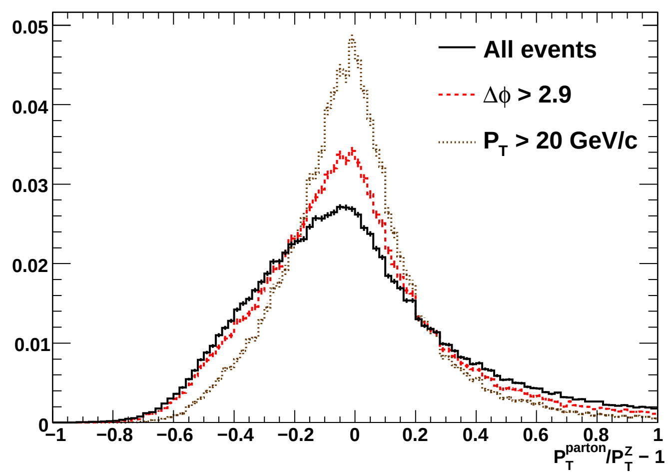

Figure 5–4: p_T balance distributions at parton level for simulated Z + Jet events. Imposing a $\Delta\phi$ cut reduces the asymmetry and tails of the distribution. The asymmetry and tails are further reduced by requiring a minimum p_T for the Z and parton. The three distributions are normalised to the same number of events.

in this work will employ minimum p_T requirements above the simulation sample $\hat{p_T}$ threshold.

The analysis algorithm described in Section 5.2.1 was applied to the Z + Jet simulation data at parton level. Selected events were required to have $\Delta\phi > 2.8$, and the lowest p_T^Z bin was chosen to be 20 to 30 GeV/c. The p_T balance as a function of p_T^Z is shown in Figure 5–5. From this plot, two kinematic regions can be identified. In the region where $p_T^Z > 60$ GeV/c, the balance has very little dependence on p_T^Z, and is within 2% of perfect balance. The exception to this is at higher p_T (> 300 GeV/c), where the technique is limited due to the statistics of the Monte Carlo simulated sample (which represents 311 pb^{-1} of integrated luminosity). A different situation is seen in the region where $p_T^Z < 60$ GeV/c. Here, the balance is p_T^Z dependent, and is increasingly shifted towards $p_T^{parton}/p_T^Z - 1 < 0$ as p_T^Z decreases. This suggests that even with a cut on $\Delta\phi$, at low p_T^Z there is a measurable influence from the initial p_T of the interaction on the p_T balance.

The reason why the balance of events with low p_T are most affected by the initial p_T of the interaction can be explained kinematically. The p_T balance will experience the largest deviation from 0 when the magnitude of initial p_T is of the same order (or larger) as the p_T of the Z boson or parton, and is in the same direction as the Z boson or parton. Figure 5–6 shows the interaction initial p_T spectrum, which has a peak near 5 GeV/c and a high energy tail which extends past 50 GeV/c. While a cut on $\Delta\phi$ helps to reduce the number of events with large initial p_T, it does not completely eliminate the high energy tail. This indicates that there are still a significant number of events produced with an initial $p_T > 5$ GeV/c which pass the $\Delta\phi$ requirement.

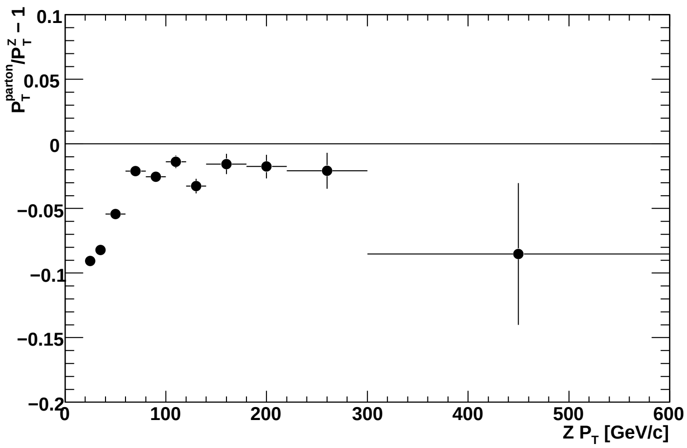

Figure 5–5: p_T balance versus p_T^Z at parton level in simulated Z + Jet events, with a $\Delta\phi > 2.8$ cut.

These events will disturb the p_T balance in the lowest p_T^Z bins to a greater extent than in the higher p_T^Z bins.

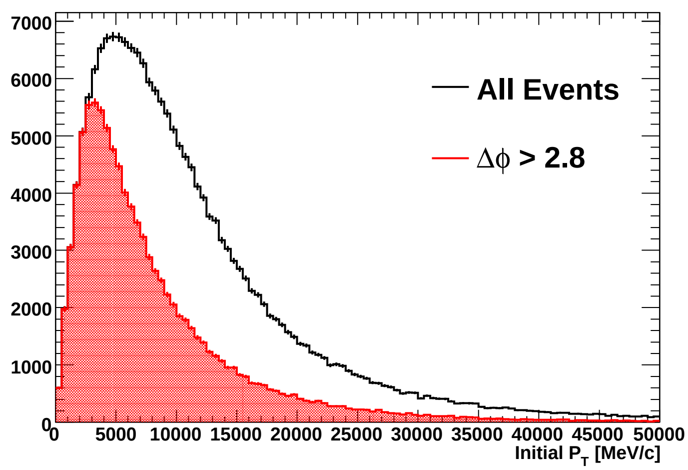

Figure 5–6: Spectrum of initial p_T for simulated Z + Jet events. Imposing a $\Delta\phi$ cut helps to remove events with large initial p_T, but is not a perfect discriminator.

5.4 p_T Balance - Reconstructed Level

At the reconstructed level, Z + Jet events are identified by applying a series of selection cuts on reconstructed physics objects. These criteria are meant to select Z + Jet events produced with minimal initial p_T, while suppressing background processes which "fake" Z + Jet events. Two similar yet separate sets of criteria were used in this analysis; one for the electron channel ($Z \rightarrow e^+e^-$) and one for the muon channel ($Z \rightarrow \mu^+\mu^-$).

5.4.1 Particle Reconstruction

Electron Identification Electron candidates are first identified in ATLAS by matching a track with an electromagnetic cluster of energy in the calorimeter. By applying a set of reference cuts on the calorimeter shower shape and tracking variables, the electron candidates can then be further classified as "loose", "medium" or "tight" electrons [11]. In going from loose to tight cuts, the background rejection of jets which fake electrons increases by a factor$\sim 10^5$, however the efficiency of identifying electrons[4] drops from $\sim 88\%$ to $\sim 62\%$. In this study, electrons were required to pass the tight reference cuts in order to reduce background contamination to a minimum.

Muon Identification Muon candidates in this analysis were identified using the Staco (STAtistical COmbination) algorithm [3], which searches for muons which leave tracks in both the muon spectrometer and inner detector. The algorithm

[4] Electron identification efficiency is defined as $\epsilon = \frac{N_e^{Id}}{N_e^{truth}}$, where N_e^{Id} is the number of ATLAS reconstructed and identified electron candidates and N_e^{truth} is the number of "true" electrons, known from simulation.

then statistically merges the two independent tracks by combining their covariance matrices. Muons reconstructed with the STACO algorithm have an identification efficiency of $\sim 95\%$.

5.4.2 Z Boson Selection

While the trigger system's principle task is to reduce the event rate to a reasonable amount for recording, it also helps to identify events by indicating which trigger signatures were passed. In the electron channel, events were required to pass a trigger signature requiring a single medium electron, with $p_T \geq 5$ GeV/c (`EF_e5_medium`). In the muon channel, events were required to pass a single muon trigger signature with $p_T \geq 10$ GeV/c (`EF_mu10`), or a di-muon trigger signature with at least one muon with $p_T \geq 4$ GeV/c (`EF_2mu4`). These particular trigger signatures were chosen as they were the lowest p_T un-prescaled signatures for electrons and muons available in the trigger menu. It is advantageous to use the lowest un-prescaled trigger signature, as it helps to ensure that the physics analysis is performed in a kinematic region where the trigger is most efficient. In this study, the trigger signatures used in the electron and muon channels were both found to have an efficiency[5] of 95%.

In both channels, at least two lepton candidates (either electrons or muons) are required in the event. Then the invariant mass of all combinations of electrons (or muons) with opposite charge is calculated. If the invariant mass of the electron/muon

[5] Here, trigger efficiency is defined as $\epsilon = \frac{N_{trig}^{passed}}{N^{passed}}$, where N_{trig}^{passed} is the number of Z + Jet events which passed all the selection criteria including trigger, and N^{passed} is the number of Z + Jet events which passed the selection criteria, with the trigger removed.

pair is within $\pm\Delta M_Z < 20$ GeV/c^2 from the Z mass, it is considered a Z candidate. For this analysis, only events with exactly one Z candidate are considered.

Once an event with exactly one reconstructed Z boson has been identified, the p_T of the reconstructed Z boson is calculated. Figure 5–7 shows a comparison between the p_T distribution of truth Z bosons (Truth Z), reconstructed Z bosons from truth decay leptons (Truth Reco Z), and reconstructed Z bosons from ATLAS reconstructed leptons (Reco Z) for the electron (Figure 5–7a) and muon (Figure 5–7b) channels. As can be seen, there is good agreement in the shape of all three distributions for both $Z \to e^+e^-$ and $Z \to \mu^+\mu^-$ + Jet events, indicating the excellent p_T reconstruction for electrons and muons at ATLAS.

The uncertainty in p_T for reconstructed Z bosons can be estimated by looking at the p_T resolution for electrons and muons. From conservation of transverse momentum, p_T^Z is reconstructed from the p_T of its decay leptons:

$$|p_T^Z|^2 = |p_T^{e/\mu,+}|^2 + |p_T^{e/\mu,-}|^2 + 2|p_T^{e/\mu,+}||p_T^{e/\mu,-}|\cos\Delta\phi \tag{5.2}$$

where $\Delta\phi$ is the azimuthal angle between decay leptons. Considering that the ϕ position resolution is much better than the p_T resolution of electrons and muons [11], and using the assumption that $\sigma(p_T^{e/\mu,-}) \approx \sigma(p_T^{e/\mu,+}))$, the resolution of p_T^Z can be expressed as:

$$\sigma(p_T^Z) \approx \sqrt{2}\sigma(p_T^{e/\mu}). \tag{5.3}$$

The p_T resolution of reconstructed electrons and muons is p_T-dependent, and varies between 2 to 6% for muons and between 5 to 1% for electrons[6] across a p_T range of 10 to 200 GeV/c [11]. From Equation (5.3), the p_T^Z resolution is then expected to be within 2 to 8%. In Figure 5–7, this resolution effect is manifest as a smearing of reconstructed p_T^Z by a few GeV/c.

5.4.3 Leading Jet Selection

The jet with the highest transverse momentum in the event was selected to balance against the Z boson. To avoid misidentification, any jets which overlapped with the leptons from the Z decay within a $\Delta R < 0.1$ were removed from the event. In this study, only events where the leading jet fell into the region of the electromagnetic and hadronic barrel calorimeter with tracking information ($|\eta| < 2.5$), but not in the "crack" region between the barrel and end-cap ($1.3 < |\eta| < 1.6$), were considered. In addition to cuts on $|\eta|$, the leading jet was also required to have a $p_T^{min} > 20$ GeV/c. A cut on p_T^{min} aims to reduce the influence from soft jets originating from outside the Z + Jet process (i.e. underlying event, pileup, noise), as well as any bias from the $\hat{p_T}$ threshold. Finally, the leading jet was required to be isolated by not having another jet within $\Delta R < 1.0$. The isolation requirement attempts to remove events where the leading jet has undergone gluon radiation [32].

[6] At higher p_T, the p_T resolution improves for electrons and degrades for muons. This is because electron momentum is measured using calorimetry, which has a resolution which improves with energy. Muon momentum is determined using the curvature from tracking information, which has a resolution which degrades at high p_T as the tracks become less curved.

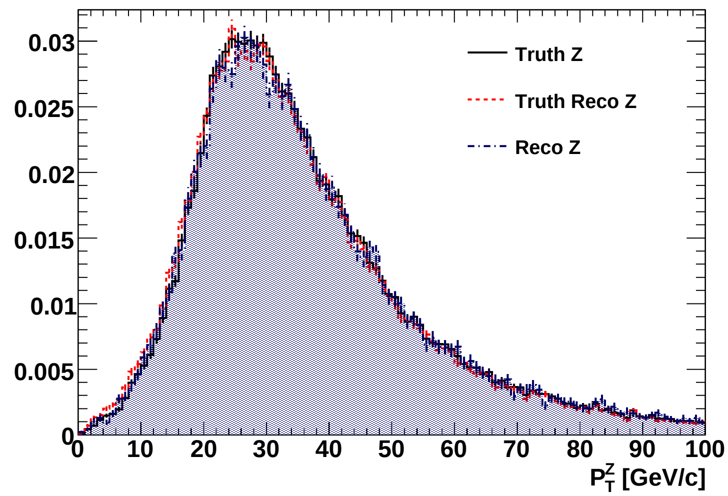

(a) $Z \rightarrow e^+e^-$

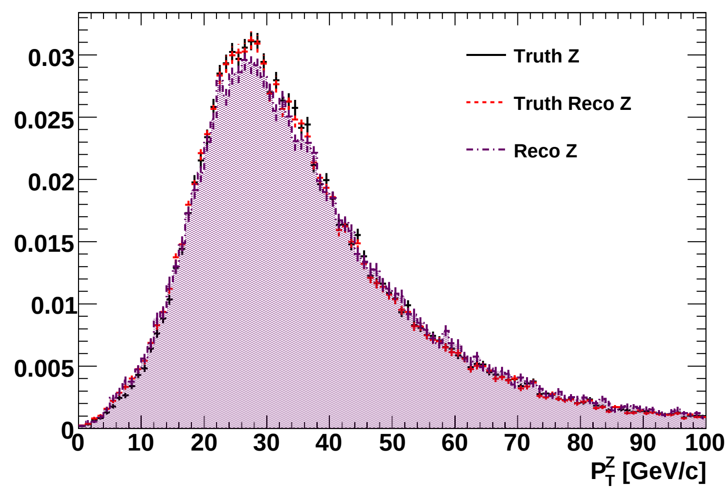

(b) $Z \rightarrow \mu^+\mu^-$

Figure 5–7: Comparison of p_T^Z distributions for simulated $Z(\rightarrow e^+e^-)$ + Jet (a) and $Z(\rightarrow \mu^+\mu^-)$ + Jet (b) events. The p_T of truth Z bosons (Truth Z), Z bosons reconstructed from truth decay leptons (Truth Reco Z), and Z bosons reconstructed from ATLAS reconstructed leptons (Reco Z) are displayed. The p_T distributions are normalised to the same number of events.

5.4.4 Event Topology

As with the parton level study, event topology cuts were used to minimise the imbalance from initial p_T effects. Events were required to have $\Delta\phi > 2.8$ between the leading jet and reconstructed Z. To further reduce the number of events with significant initial p_T, the second highest p_T jet in the event was required to have $p_T^{2ndjet} < 20$ GeV/c. The systematic variation of these selection cuts is investigated in Section 5.5.

5.4.5 p_T Balance - Truth Jets

The analysis algorithm in Section 5.2.1 with the listed selection criteria was run over the 7 TeV $Z(\rightarrow e^+e^-)$ and $Z(\rightarrow \mu^+\mu^-)+$ Jet simulation samples, which represents an integrated luminosity of 470 pb^{-1}. Figure 5–8 shows the p_T balance in bins of p_T^Z for cone jets reconstructed with $\Delta R = 0.4$ and $\Delta R = 0.7$, using truth particles as inputs to the jet algorithm. Figure 5–9 also displays the p_T balance against p_T^Z for truth jets, only using the anti-k_T algorithm with $D = 0.4$ and $D = 0.6$.

In general, the p_T balance for the narrow truth jets (cone with $\Delta R = 0.4$ and anti-k_T with $D = 0.4$) yields a value which is less than that for the wide truth jets (cone with $\Delta R = 0.7$ and anti-k_T with $D = 0.6$). This is most likely due to out-of-cone losses in the narrow jets, where energy from the parton shower falls outside of the jet radius, resulting in a measured jet energy which is less than the true parton energy. Out-of-cone losses are most significant for poorly collimated parton showers, which produce particle jets which may be larger than the size parameter of the chosen jet algorithm. In practice, high p_T jets tend to be narrower than low p_T

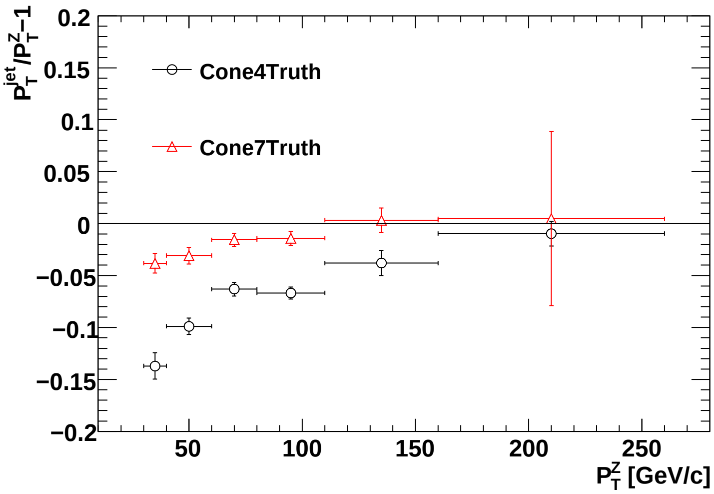

(a) $Z \to e^+e^-$

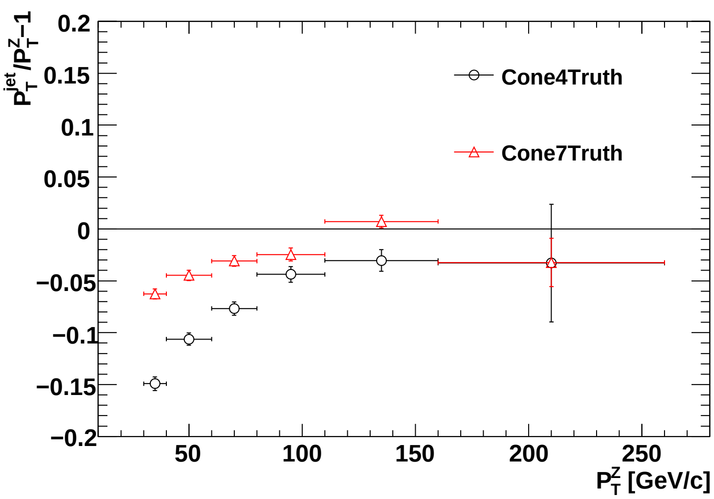

(b) $Z \to \mu^+\mu^-$

Figure 5–8: Comparison of p_T balance between $\Delta R = 0.4$ and $\Delta R = 0.7$ Cone jets using truth particles as input in simulated Z + Jet events, for Z decaying to electrons (a) and muons (b).

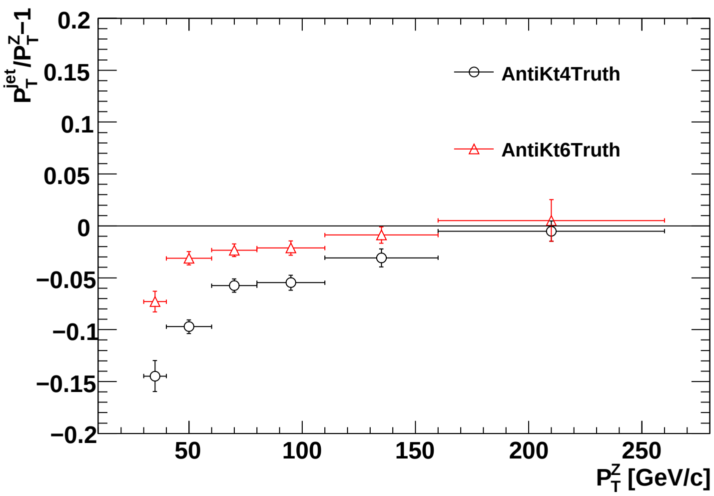

(a) $Z \to e^+e^-$

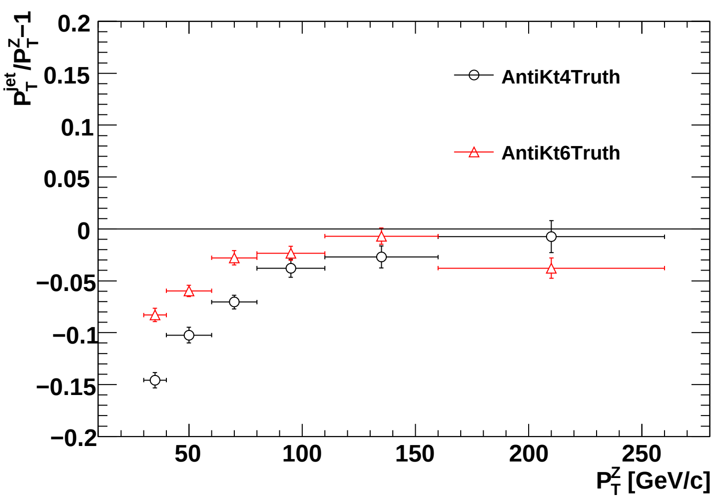

(b) $Z \to \mu^+\mu^-$

Figure 5–9: Comparison of p_T balance between $D = 0.4$ and $D = 0.6$ anti-k_T jets using truth particles as input in simulated Z + Jet events, for Z decaying to electrons (a) and muons (b).

jets, as suggested by Figure 5–10. This makes sense kinematically, as a parton with large p_T will be highly boosted, so its fragmentation and hadronisation products will also be boosted in the same direction, hence well collimated.

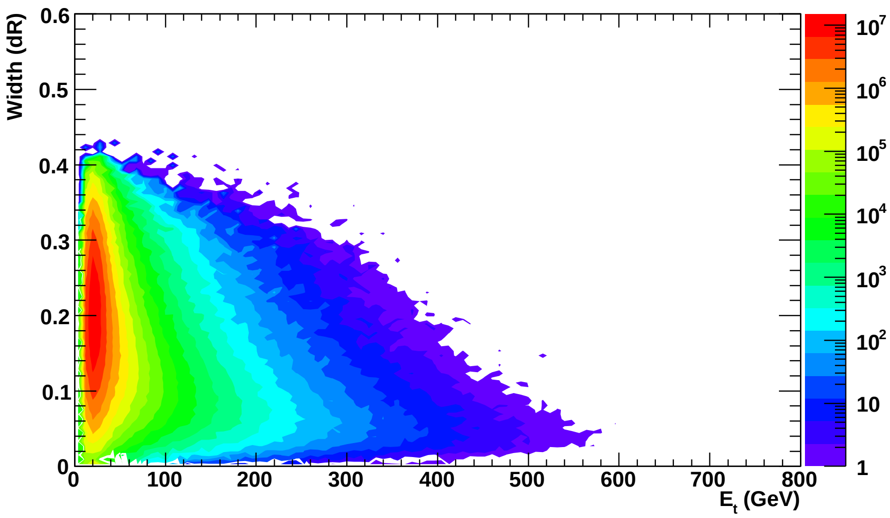

Figure 5–10: Relationship between the width (in ΔR) of a jet and jet E_T. This figure suggests that high E_T jets tend to be narrower than low E_T jets.

In addition to out-of-cone losses, narrow and wide jets can have different energies resulting from the inclusion of the underlying event in the jet. A wider jet will pull in more energy from the underlying event than a narrow jet, leading to a measured jet energy which is larger. Since the underlying event contributes hadronic activity in the calorimeter which is not from the Z + Jet process, wide jets can potentially lead to an over estimation of parton energy.

The p_T balance for narrow truth jets has a p_T^Z dependence, with the dependence most pronounced for $p_T^Z < 60$ GeV/c. The wide truth jets also give a p_T balance which is p_T^Z dependent in this region, however the effect is not as strong. From the parton level study (Section 5.3), this is the same kinematic region where the initial p_T of the interaction has the greatest influence on the p_T balance.

For wide truth jets, the p_T balance as a function of p_T^Z follows a very similar shape to that of the parton level study. In the $p_T^Z > 60$ GeV/c range, the p_T balance values of the wide truth jets are within 3% of perfect balance, as was the case at parton level. This result suggests that indeed, there is a bias in the p_T balance at $p_T^Z < 60$ GeV/c due to the initial p_T of the interaction. At larger p_T^Z, this bias diminishes to 2-3%, but is not entirely eliminated. This suggests that p_T balancing in Z + Jet events is not a good *in situ* technique for precise knowledge of the jet calibration performance. The technique is still useful, however, for a general study of jet calibration performance. For the remainder of this analysis, the p_T balance in the $p_T^Z < 60$ GeV/c region will still be shown in order to show relative differences, however the deviation of the balance from 0 is to be expected.

5.5 Estimate of Systematics

In order to properly understand the performance of the jet calibration using p_T balancing, it is important to see how sensitive the balance is to variations in the Z + Jet selection cuts. The following figures were made using the 7 TeV $Z(\rightarrow e^+e^-)$ and $Z(\rightarrow \mu^+\mu^-)+$ Jet simulation samples. All jets were reconstructed with the $\Delta R = 0.7$ cone algorithm, and using H1 calibrated topological towers as inputs.

5.5.1 $\Delta\phi$ Cut

In Figure 5–11, the p_T balance is shown with the cut on $\Delta\phi$ varied between > 0 (no cut), 2.7, 2.8 and 2.9 radians. For the samples selected *with* a cut on $\Delta\phi$, the difference in p_T balance between them was found to be within statistical errors

(2%). The $\Delta\phi$ cut appears to have the most significant effect at low p_T^Z (< 60 GeV/c), where there is the largest variation in p_T balance. As shown in the parton level study, this is also the kinematic region where effects from initial p_T are the strongest. The tightest cut ($\Delta\phi > 2.9$) gave a balance which is slightly closer to 0 in the low p_T^Z region, with a modest loss of statistics.

5.5.2 ΔM_Z Cut

Figure 5–12 shows the variation of p_T balance for events with different cuts on ΔM_Z. The purpose of this cut is to reduce the number of combinatoric pairs of electrons or muons which have an invariant mass which happens to be close to $M_Z = 91.2$ GeV/c^2, "faking" a reconstructed Z boson. Varying this cut on the signal data had a negligible effect on the p_T balance, with all values agreeing to within their statistical errors.

5.5.3 Leading Jet p_T Cut

Underlying event and noise mainly affect jets at low p_T ($<$ 20 GeV/c) [10]. This cut sets the minimum p_T for a leading jet in an event to be used in calculating the p_T balance. If the cut is set too high relative to the lowest p_T^Z bins, it can seriously bias the balance in those bins, as shown in Figure 5–13. This happens because the cut removes the lowest p_T jets in the bin, giving an asymmetric p_T balance distribution in that bin. The remaining events in the bin tend to have a leading jet with larger p_T than the Z boson, biasing the p_T balance to be a larger value. This effect is evident in the 30 GeV/c $< p_T^Z <$ 40 GeV/c bin, for the $p_T^{lead} >$ 30 GeV/c cut.

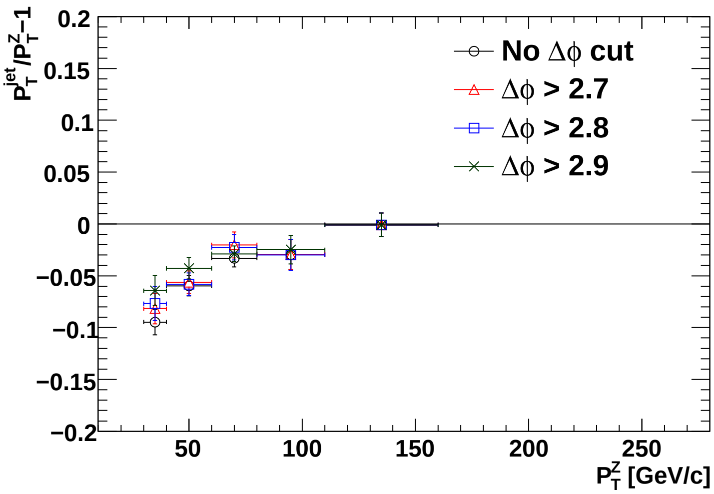

(a) $Z \to e^+e^-$

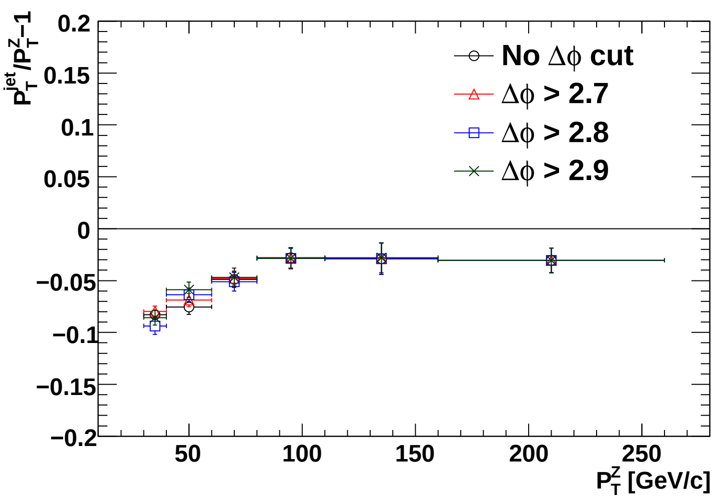

(b) $Z \to \mu^+\mu^-$

Figure 5–11: Comparison of p_T balance vs p_T^Z for various selection cuts on $\Delta\phi$ in simulated Z + Jet events, for Z decaying to electrons (a) and muons (b).

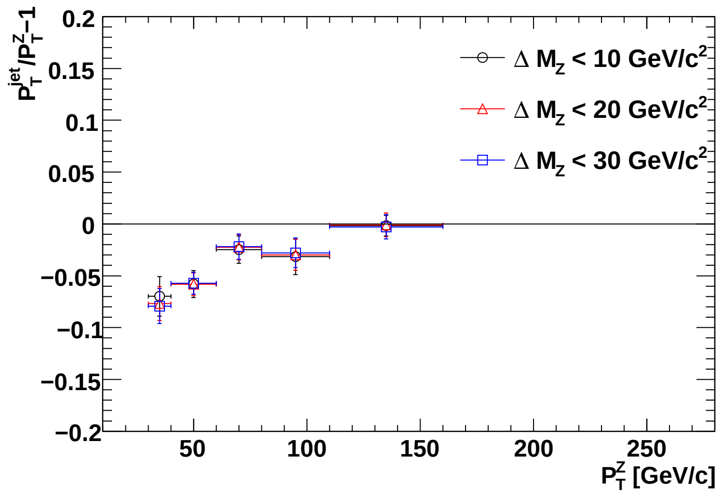

(a) $Z \to e^+e^-$

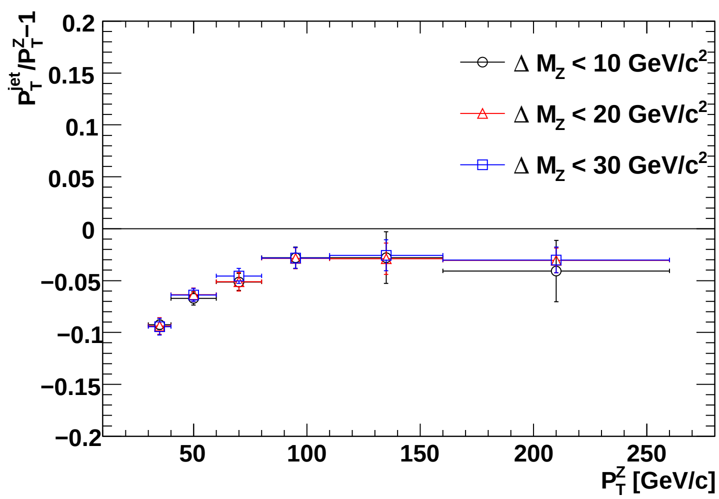

(b) $Z \to \mu^+\mu^-$

Figure 5–12: Comparison of p_T balance vs p_T^Z for various selection cuts on ΔM_Z in simulated Z + Jet events, for Z decaying to electrons (a) and muons (b).

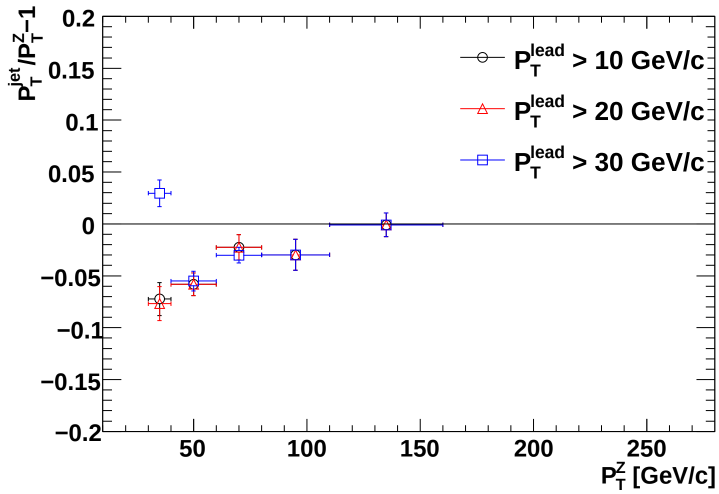

(a) $Z \to e^+e^-$

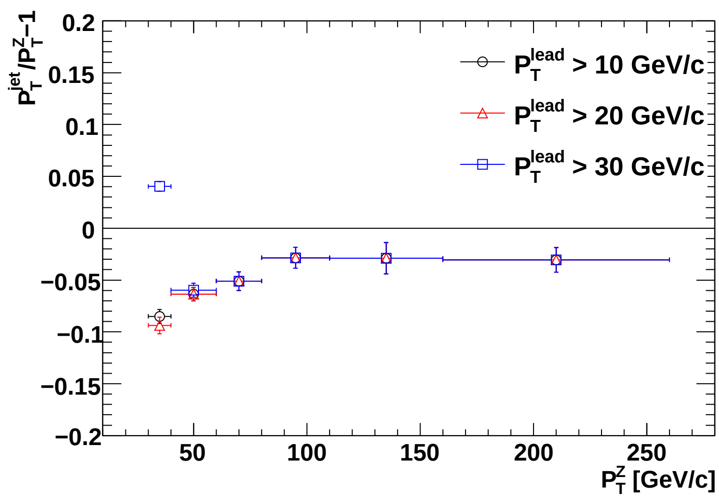

(b) $Z \to \mu^+\mu^-$

Figure 5–13: Comparison of p_T balance vs p_T^Z for various selection cuts on the minimum leading jet $p_T$in simulated Z + Jet events, for Z decaying into electrons (a) and muons (b).

5.5.4 Second Leading Jet p_T Cut

The cut on the maximum p_T of the second leading jet attempts to eliminate events with significant hadronic activity outside of the Z + Jet hard process (namely, events with large interaction initial p_T). Figure 5–14 displays the effect of varying the maximum p_T^{2ndjet} limit on the p_T balance. This p_T^{2ndjet} cut has a relatively small effect on the p_T balance, with all results agreeing within statistical errors (up to 4%).

The cut produces the largest variation in the balance at high p_T^Z. Interestingly, the tightest cut of $p_T^{2ndjet} < 10$ GeV/c removes the most statistics from the high p_T^Z bins, but in the case of the $Z \rightarrow e^+e^-$ channel (Figure 5–14a), it yields a stable gaussian fit to the p_T balance distribution, while the more relaxed p_T^{2ndjet} cuts have an unstable fit. This is due to the tight p_T^{2ndjet} cut removing events where the energetic second leading jet disturbs the p_T balance distribution, leaving a distribution which is more Gaussian-like.

5.5.5 $|\eta|$ Crack Cut

Jets which fall into the calorimeter $|\eta|$ "crack" region ($1.3 < |\eta| < 1.6$) are expected to have a poor energy resolution and calibration performance, due to undetected or partially detected particle energy. Figure 5–15 shows the effect of removing events where the leading jet has landed in the calorimeter $|\eta|$ crack region on the p_T balance, as a function of p_T^Z. This cut has a negligible influence on the balance, with a difference of less than 1% between samples with and without the cut. The effect of cutting the $|\eta|$ crack region is more evident in Figure 5–16, where the p_T balance is plotted against η of the leading jet.

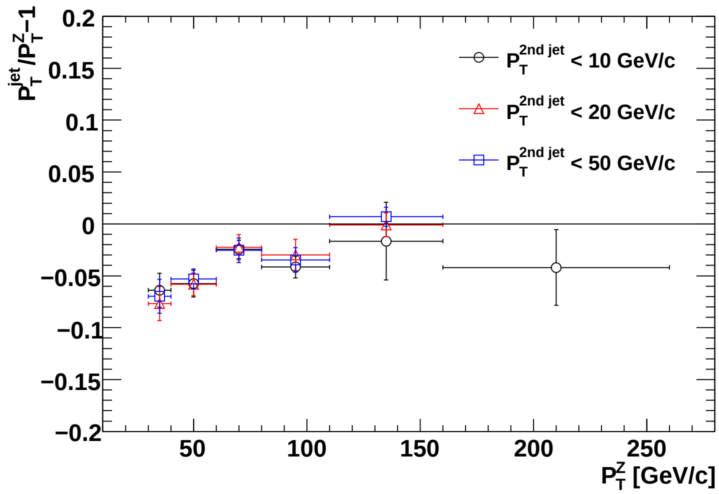

(a) $Z \rightarrow e^+e^-$

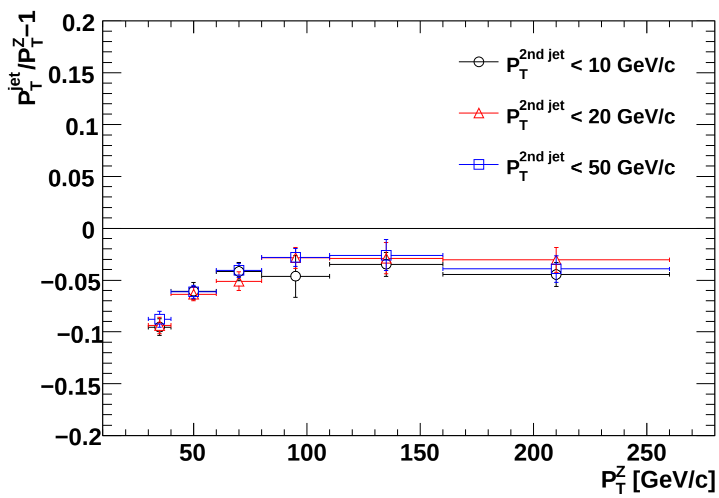

(b) $Z \rightarrow \mu^+\mu^-$

Figure 5–14: Comparison of p_T balance vs p_T^Z for various selection cuts on the maximum second leading jet p_T in simulated Z + Jet events, for Z decaying into electrons (a) and muons (b).

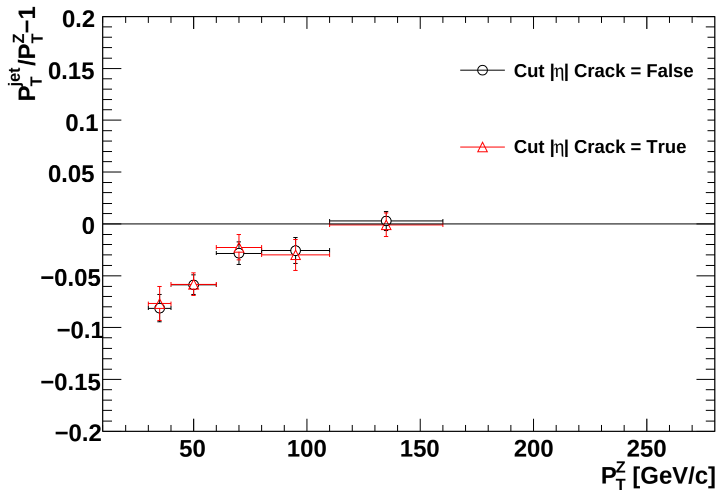

(a) $Z \rightarrow e^+e^-$

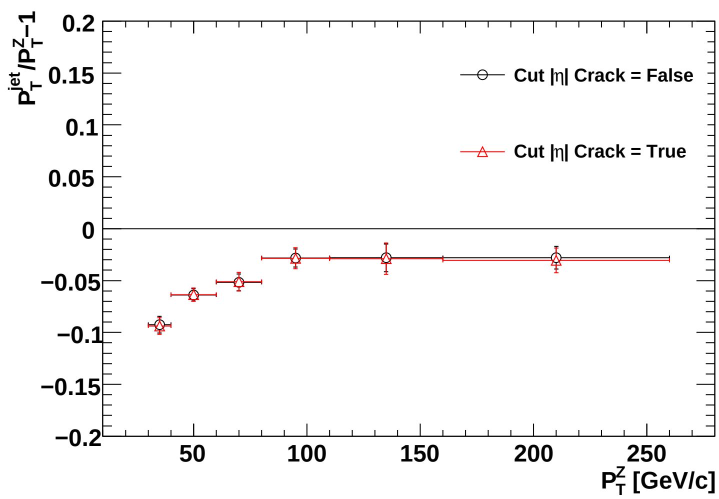

(b) $Z \rightarrow \mu^+\mu^-$

Figure 5–15: Comparison of p_T balance vs p_T^Z between simulation Z + Jet samples, where if the leading jet fell in the calorimeter crack region ($1.3 < |\eta| < 1.6$), the event was either kept (Cut $|\eta|$ Crack = False) or rejected (Cut $|\eta|$ Crack = True). Plots are shown for Z decaying into electrons (a) and muons (b).

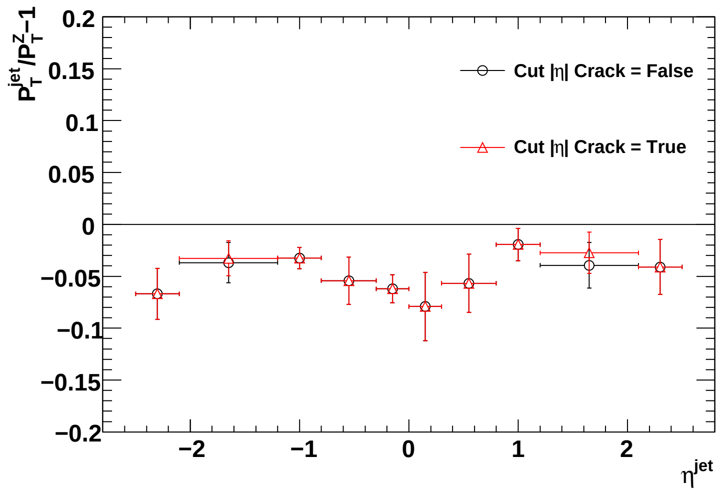

(a) $Z \to e^+e^-$

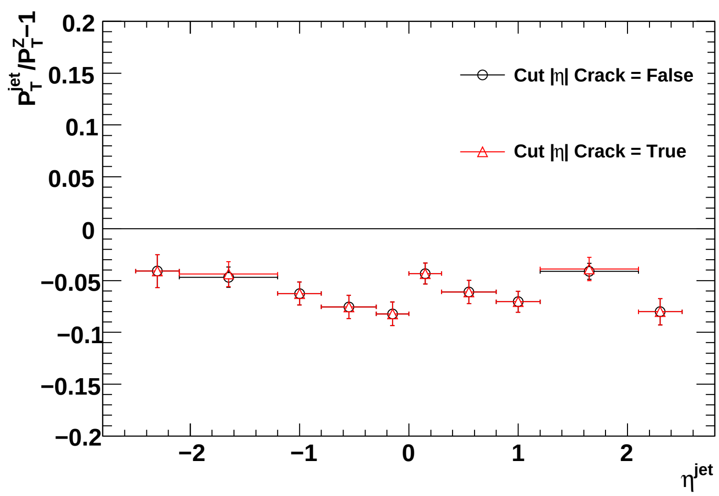

(b) $Z \to \mu^+\mu^-$

Figure 5–16: Comparison of p_T balance vs η^{jet} between simulation Z + Jet samples, where if the leading jet fell in the crack region ($1.3 < |\eta| < 1.6$), the event was either kept (Cut $|\eta|$ Crack = False) or rejected (Cut $|\eta|$ Crack = True). Plots are shown for Z decaying into electrons (a) and muons (b).

5.5.6 Electron PID

In the $Z \rightarrow e^+e^-$ channel, the electrons used to reconstruct the Z boson must meet certain identification criteria, known as "loose", "medium" or "tight" criteria. Figure 5–17 shows the p_T balance for $Z(\rightarrow e^+e^-)$ + Jet events using the three different electron selection criteria. All three samples give p_T balance values which agree to within their statistical uncertainty ($\sim 2\%$). The "loose" electron sample yields the largest number of statistics, but is expected to have the greatest contamination from background processes (namely, dijet events).

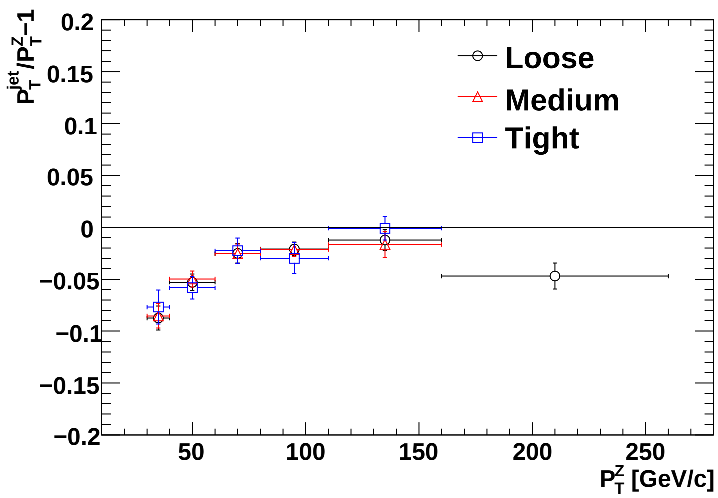

Figure 5–17: Comparison of p_T balance vs p_T^Z for simulated $Z(\rightarrow e^+e^-)$ + Jet events, with the Z boson reconstructed from "loose", "medium" or "tight" electrons.

5.6 Backgrounds to Z + Jet Events

In real collisions, detecting the Z + Jet signal will be more difficult as there are background processes which can mimic a Z + Jet event. The processes listed in Tables 5–2 and 5–3 were considered as the dominant backgrounds to $Z(\rightarrow e^+e^-)$ and $Z(\rightarrow \mu^+\mu^-)$ + Jet events, as investigated in [11] and [33]. To accommodate the differing cross sections of each process, the samples were normalised to an integrated luminosity of 100 pb^{-1}. Once normalised, the analysis algorithm with nominal selection cuts was run over both signal and background processes. Table 5–4 lists the number of events for each process which passed the selection criteria, along with statistical uncertainties. The estimated statistical uncertainties are representative of the size of the simulation samples used in this study, and do not represent the expected statistical uncertainties for 100 pb^{-1} of data.

Table 5–4: Expected number of events for Z + Jet signal and background processes in 100 pb^{-1} of data after selection cuts. Note the estimated statistical uncertainties are representative of the size of the simulation samples used.

Process	Events Accepted	Sample Composition (%)
$\mathbf{Z \rightarrow e^+e^- +}$ **Jet**	$\mathbf{3145 \pm 31}$	$\mathbf{100 \pm 1}$
$t\bar{t} \rightarrow l + X$	1.0±0.3	0.03±0.01
QCD (dijet)	0.10±0.07	0.003±0.002
$\mathbf{Z \rightarrow \boldsymbol{\mu}^+\boldsymbol{\mu}^- +}$ **Jet**	$\mathbf{6673 \pm 46}$	$\mathbf{94 \pm 1}$
QCD ($b\bar{b} \rightarrow \mu\mu + X$)	397±55	5.6±0.8
$W \rightarrow \mu\nu +$ Jet	21±9	0.3±0.1
$t\bar{t} \rightarrow l + X$	0.8±0.3	0.011±0.004

In the electron channel, the background processes were virtually eliminated by the signal selection requirements. It is difficult to draw conclusions about the dijet background, however, as very few events survived the cuts. Given the large QCD cross section compared to Z + Jet events (see Table 5–2), further study should be done using a dijet sample with larger statistics. That being said, the high jet rejection of the "tight" electron criteria ($\sim 10^5$) should ensure very little QCD background. The requirement of using "tight" electrons is also the reason why the number of statistics in the $Z(\rightarrow e^+e^-)$ + Jet channel is much smaller than in the $Z(\rightarrow \mu^+\mu^-)$ + Jet channel.

In the muon channel, the dominant background was from QCD ($b\bar{b} \rightarrow \mu\mu + X$) events, which composed $\sim 6\%$ of the events passing the selection criteria. The muons from this process originate from the decay of B mesons, which are typically boosted in the lab frame. This leads to the collimation of all of the B meson decay products, in what is called a "b-jet". As such, the muons from this process are typicially not isolated. It has been shown that the contamination from QCD ($b\bar{b} \rightarrow \mu\mu + X$) events can be reduced further by requiring the muons to be isolated [33, 34]. This was not investigated in this study.

The systematic shift of the p_T balance due to the presence of background processes can be estimated from:

$$\delta B_{bkg} = \frac{B^{bkg+S} - B^S}{B^S} \tag{5.4}$$

where B^S is the balance calculated from signal events, and B^{bkg+S} is the balance calculated from all events (signal + backgrounds). As shown in Figure 5–18, the shift in p_T balance due to the presence of the studied background events is negligible ($< 1\%$).

In general, the systematic effects on the p_T balance in Z + Jet events from varying selection cuts and the contribution from background processes is small ($<$ 4%, and $< 2\%$ in most cases), and the results are stable.

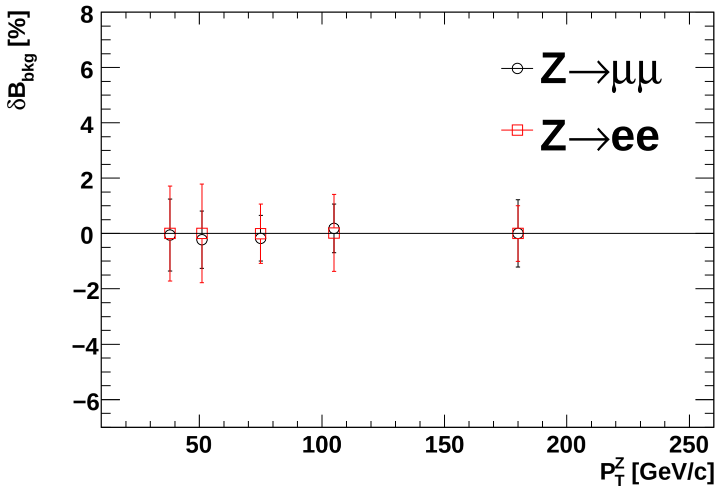

Figure 5–18: Systematic shift of p_T balance due to Z + Jet background processes.

CHAPTER 6
Jet Reconstruction and Calibration Performance

The Z + Jet p_T balance analysis established in the previous chapter can now be used to look at the performance of jet reconstruction and calibration at ATLAS. Since there are a number of factors which can change the measured energy of a jet, the p_T balance was investigated for jets built with different input constituents, algorithms, sizes and calibrations. This analysis was performed over the $\sqrt{(}s) = 7$ TeV simulation datasets. Given the expected cross section for these processes (134 pb) and the total number of simulated events (63000), from Equation (1.1) these datasets represent 470 pb^{-1} of integrated luminosity.

6.1 Effect of Jet Input

Two possible inputs to jet reconstruction were studied using the p_T balance technique, namely topological towers and topological clusters. To compare the jets built using these inputs, the jets had the same calibration technique applied. As the local hadronic calibration does not exist for topological towers, the two jet collections were calibrated using the H1 technique. Figure 6–1 shows the difference in p_T balance bewteen H1 calibrated cone jets with $\Delta R = 0.4$ and $\Delta R = 0.7$, built from topological towers or topological clusters, and Figure 6–2 shows the same only for anti-k_T jets with $D = 0.4$ and $D = 0.6$.

For the jets reconstructed using the cone algorithm, the jets built from topological clusters appear to have p_T balance values which are larger and closer to 0 than

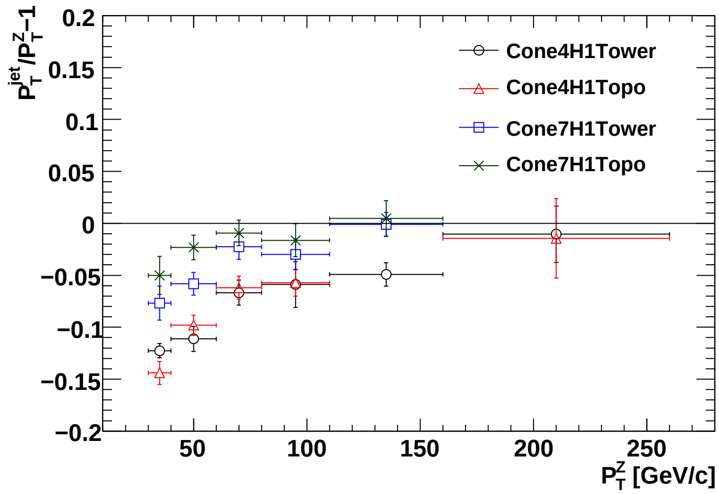

(a) $Z \to e^+e^-$

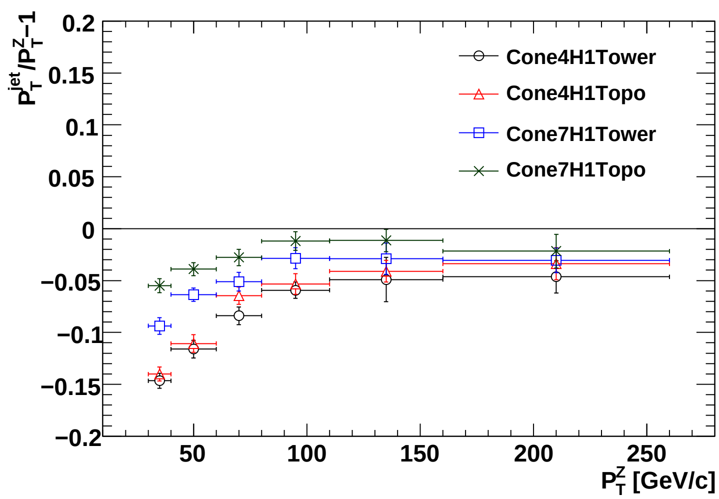

(b) $Z \to \mu^+\mu^-$

Figure 6–1: Comparison of p_T balance vs p_T^Z for H1 calibrated cone jets with $\Delta R = 0.4$ and $\Delta R = 0.7$, built from topological towers (H1Tower) or topological clusters (H1Topo). Plots are for simulated $Z(\to e^+e^-)$ + Jet (a) and $Z(\to \mu^+\mu^-)$ + Jet (b) events.

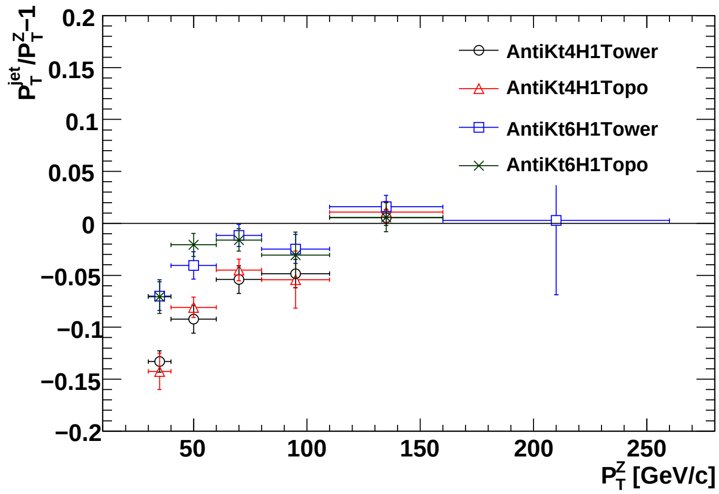

(a) $Z \to e^+e^-$

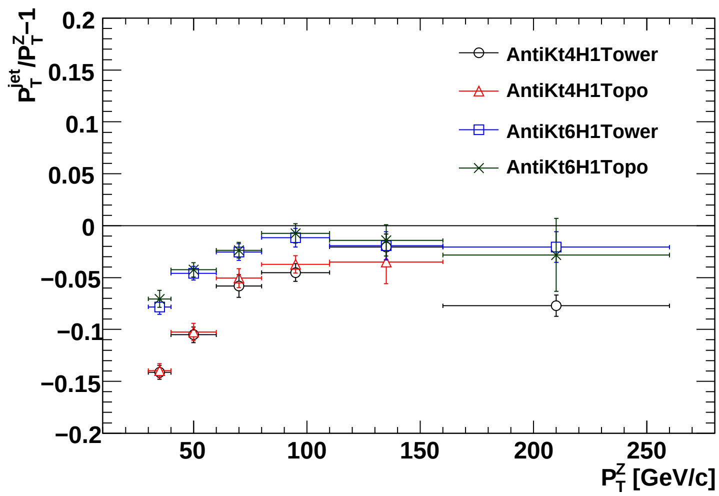

(b) $Z \to \mu^+\mu^-$

Figure 6–2: Comparison of p_T balance vs p_T^Z for H1 calibrated anti-k_T jets with $D = 0.4$ and $D = 0.6$, built from topological towers (H1Tower) or topological clusters (H1Topo). Plots are for simulated $Z(\to e^+e^-)$ + Jet (a) and $Z(\to \mu^+\mu^-)$ + Jet (b) events.

the jets built from topological towers, for both $Z(\rightarrow e^+e^-)$ and $Z(\rightarrow \mu^+\mu^-)$ + Jet events. This difference is more noticeable in the wide $\Delta R = 0.7$ cone jets. For the jets reconstructed using the anti-k_T algorithm, the difference in p_T balance for the two inputs follows the same trend as with the cone jets, however the effect is much smaller.

This difference in p_T balance is most likely due to how topological towers and topological clusters match the shape of the hadronic shower, hence how well they estimate the deposited energy from a jet. The ability of topological clusters to group cells laterally (i.e. in an unfixed range of $\eta \times \phi$) in the calorimeter allows them more flexibility in shape than for topological towers. It appears that the anti-k_T algorithm is less sensitive to this effect, most likely attributable to its unfixed ΔR range compared to the cone algorithm. For the remainder of this analysis, only topological clusters will be used as inputs to jets.

6.2 Effect of Jet Calibration

As mentioned in Section 3.3.1, the two principle jet calibration schemes used at ATLAS are the cell energy density (H1) method and the local hadronic method, along with the global re-scaling correction. Figures 6–3 to 6–6 show the p_T balance for cone and anti-k_T jets built with topological clusters as input, using the H1 and local hadronic calibration schemes plus global re-scaling. In addition to these calibrations, uncalibrated jets with the global re-scaling correction applied are also shown.

As a general trend, for all jet algorithms and sizes, the uncalibrated jets with the global re-scaling correction typically give the largest values of p_T balance. The jets with the local hadronic calibration and global re-scaling typically give the smallest values of p_T balance, and jets calibrated with the H1 technique plus global re-scaling have p_T balance values which are usually in between the other two calibration schemes. The differences in p_T balance using jets with these calibration schemes depends on the choice of jet algorithm. Jets reconstructed with the cone algorithm are much more sensitive to the calibration technique, with differences in p_T balance as large as 6% in certain p_T^Z bins. In contrast to this, jets reconstructed with the anti-k_T algorithm have p_T balance values between the various jet calibration methods which agree to within their statistical uncertainties (up to 3%).

6.3 Effect of Jet Algorithm and Size

The effect of reconstructed jet size on the p_T balance was investigated. The comparison of p_T balance for narrow and wide jets is shown in Figures 6–7 and 6–8 for jets reconstructed using the cone and anti-k_T algorithms, respectively. All jets were built using local hadronically calibrated topological clusters as inputs, with a global re-scaling correction applied.

As noticed in the study with truth jets (Section 5.4.5), wider jets tend to give p_T balance values which are larger than that for narrow jets, with the effect most dramatic at lower p_T^Z. As previously mentioned, this is most likely due to out-of-cone losses in the narrow jets.

To look at the difference in p_T balance for various jet algorithms, jets reconstructed with the cone and anti-k_T algorithm were compared with each other, grouped as narrow or wide jets (see Figures 6–9 and 6–10). All jets were built using local hadronically calibrated topological clusters as inputs, with a global re-scaling

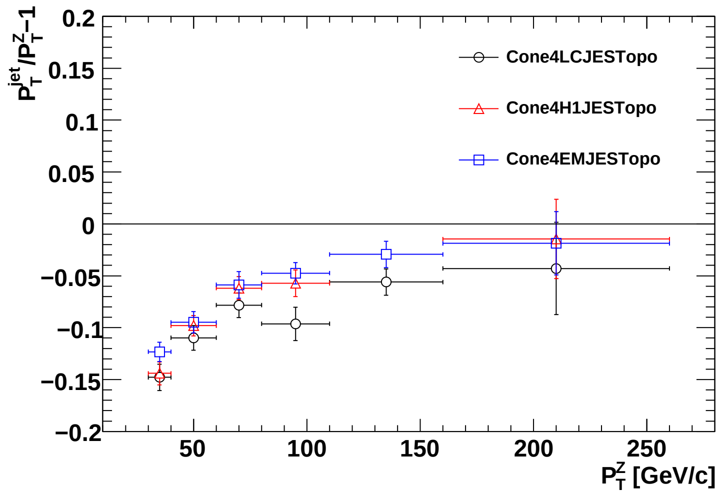

(a) $Z \to e^+e^-$

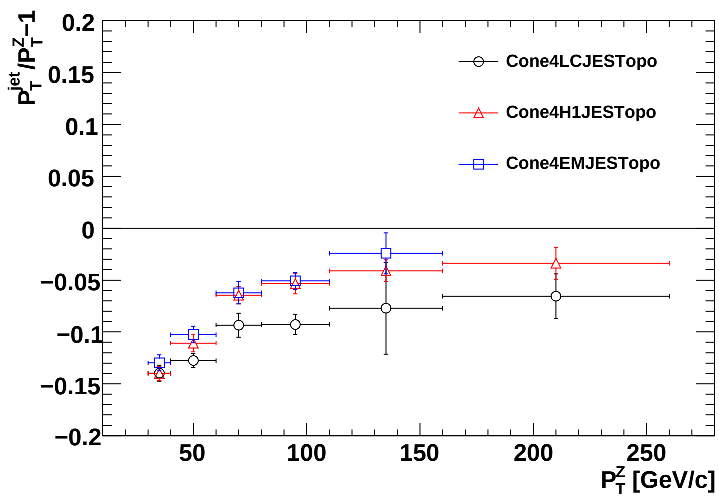

(b) $Z \to \mu^+\mu^-$

Figure 6–3: Comparison of p_T balance vs p_T^Z for cone $\Delta R = 0.4$ jets using topological clusters as input, with the following calibration schemes: H1 plus global re-scaling (H1JESTopo), local hadronic plus global re-scaling (LCJESTopo) or uncalibrated plus global re-scaling (EMJESTopo). Plots are for simulated $Z(\to e^+e^-)$ + Jet (a) and $Z(\to \mu^+\mu^-)$ + Jet (b) events.

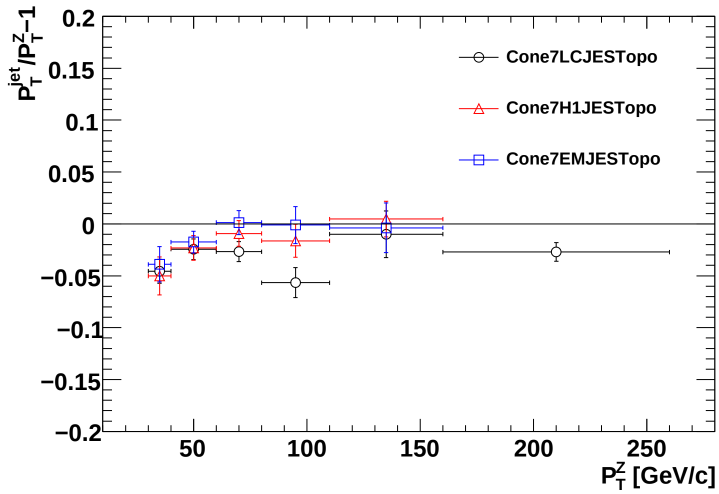

(a) $Z \to e^+e^-$

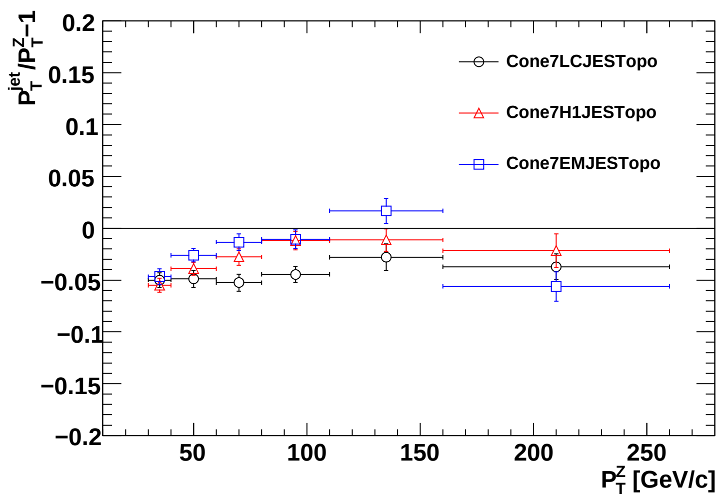

(b) $Z \to \mu^+\mu^-$

Figure 6–4: Comparison of p_T balance vs p_T^Z for cone $\Delta R = 0.7$ jets using topological clusters as input, with the following calibration schemes: H1 plus global re-scaling (H1JESTopo), local hadronic plus global re-scaling (LCJESTopo) or uncalibrated plus global re-scaling (EMJESTopo). Plots are for simulated $Z(\to e^+e^-)$ + Jet (a) and $Z(\to \mu^+\mu^-)$ + Jet (b) events.

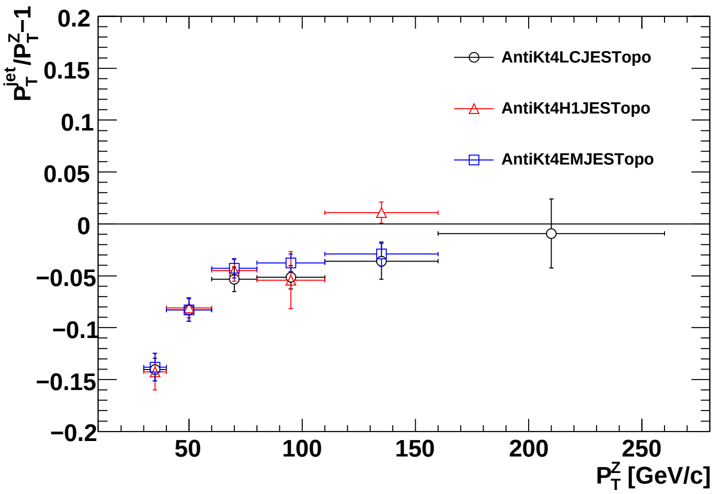

(a) $Z \to e^+e^-$

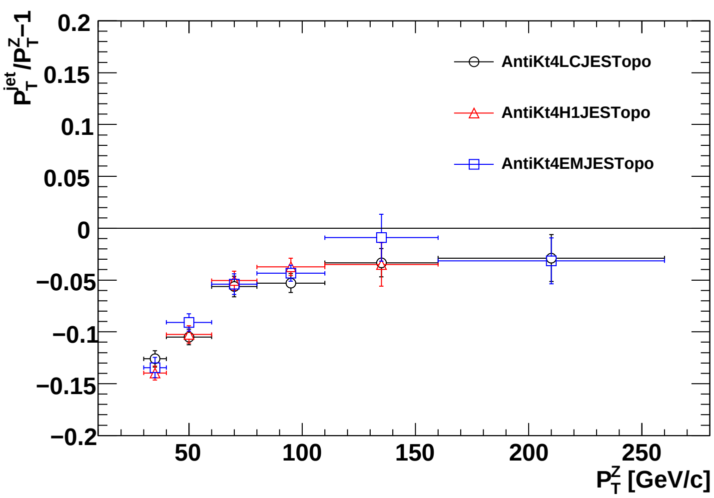

(b) $Z \to \mu^+\mu^-$

Figure 6–5: Comparison of p_T balance vs p_T^Z for anti-k_T $D = 0.4$ jets using topological clusters as input, with the following calibration schemes: H1 plus global re-scaling (H1JESTopo), local hadronic plus global re-scaling (LCJESTopo) or uncalibrated plus global re-scaling (EMJESTopo). Plots are for simulated $Z(\to e^+e^-)$ + Jet (a) and $Z(\to \mu^+\mu^-)$ + Jet (b) events.

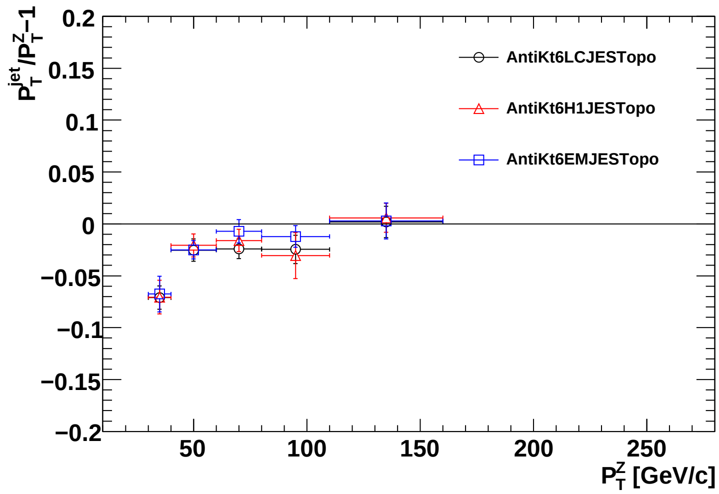

(a) $Z \to e^+e^-$

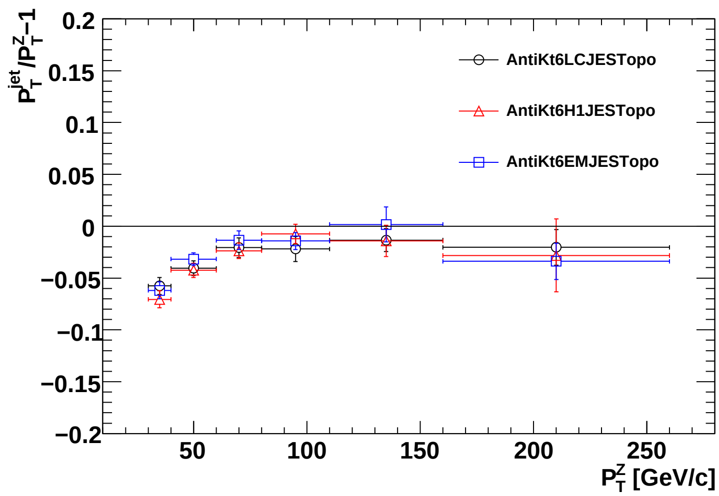

(b) $Z \to \mu^+\mu^-$

Figure 6–6: Comparison of p_T balance vs p_T^Z for anti-k_T $D = 0.6$ jets using topological clusters as input, with the following calibration schemes: H1 plus global re-scaling (H1JESTopo), local hadronic plus global re-scaling (LCJESTopo) or uncalibrated plus global re-scaling (EMJESTopo). Plots are for simulated $Z(\to e^+e^-)$ + Jet (a) and $Z(\to \mu^+\mu^-)$ + Jet (b) events.

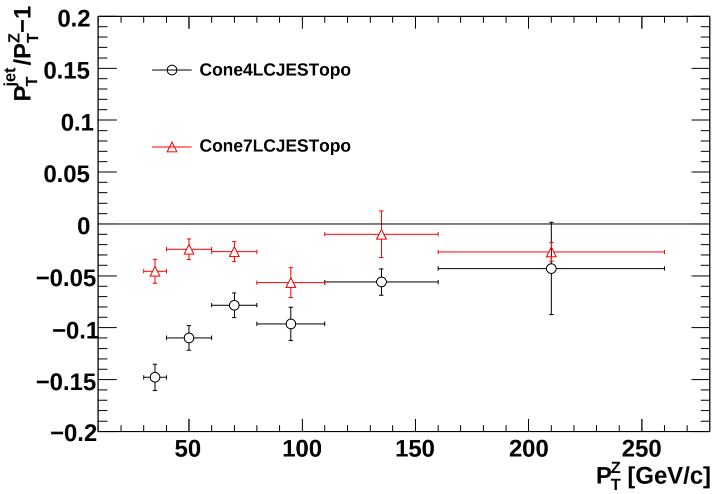

(a) $Z \to e^+e^-$

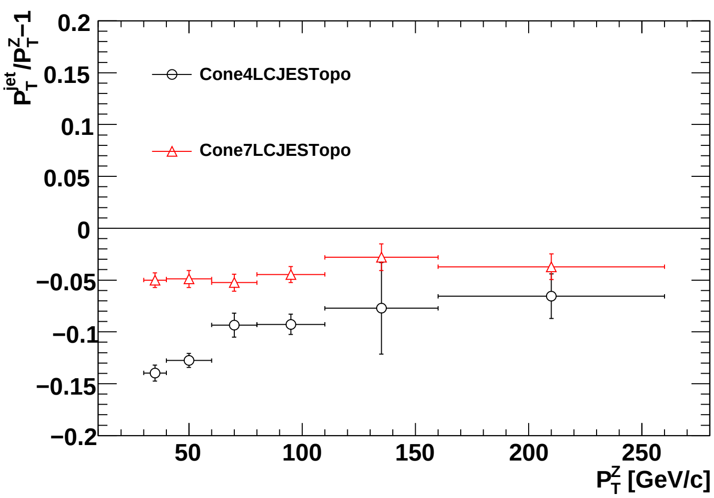

(b) $Z \to \mu^+\mu^-$

Figure 6–7: Comparison of p_T balance vs p_T^Z for wide and narrow local hadronically calibrated cone jets using topological clusters as input. Plots are for simulated $Z(\to e^+e^-)$ + Jet (a) and $Z(\to \mu^+\mu^-)$ + Jet (b) events.

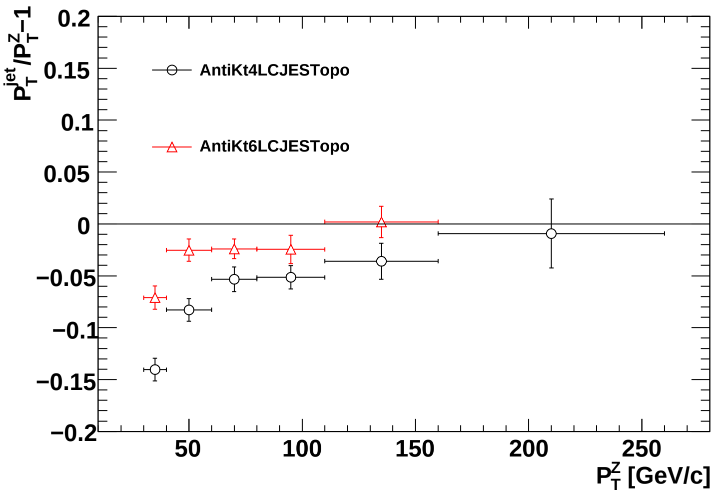

(a) $Z \to e^+e^-$

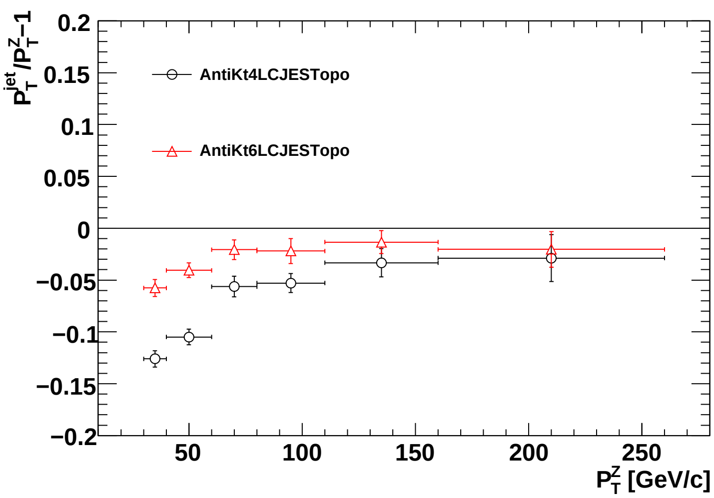

(b) $Z \to \mu^+\mu^-$

Figure 6–8: Comparison of p_T balance vs p_T^Z for wide and narrow local hadronically calibrated anti-k_T jets using topological clusters as input. Plots are for simulated $Z(\to e^+e^-)$ + Jet (a) and $Z(\to \mu^+\mu^-)$ + Jet (b) events.

correction applied. In the case of the narrow jets, the balance from the cone and anti-k_T jets agree to within 4% in both $Z(\rightarrow e^+e^-)$ and $Z(\rightarrow \mu^+\mu^-)$ + Jet events, with the anti-k_T jets giving the larger p_T balance values. The wide cone and anti-k_T jets typically have better agreement, to within less than 3%.

6.4 Performance of Reconstructed versus Truth Jets

To test the performance of the jet reconstruction, the p_T balance using reconstructed and truth jets was compared. The "best" reconstructed jet was defined as the combination of jet input and calibration whose p_T balance values most closely matched those obtained using truth jets, for a given jet algorithm. This comparison only looked at the wide cone and anti-k_T jets, as they most closely reflected the parton level p_T balance (see Figure 5–5).

The $\Delta R = 0.7$ cone jet with the best performance is the H1 calibrated jet with global re-scaling, with topological clusters as input, as shown in Figure 6–11. All values of p_T balance between the reconstructed and truth cone jets agree to within statistical uncertainties ($< 2\%$). Figure 6–12 shows the p_T balance of the best performing $D = 0.6$ anti-k_T jet, reconstructed with global re-scaled local hadronically calibrated topological clusters as input. The agreement of p_T balance values with truth $D = 0.6$ anti-k_T jets is within statistical uncertainties ($< 2\%$), with the exception of the lowest p_T^Z bins in the $Z(\rightarrow \mu^+\mu^-)$ channel. Even in this region, the differences in balance are less than 3%.

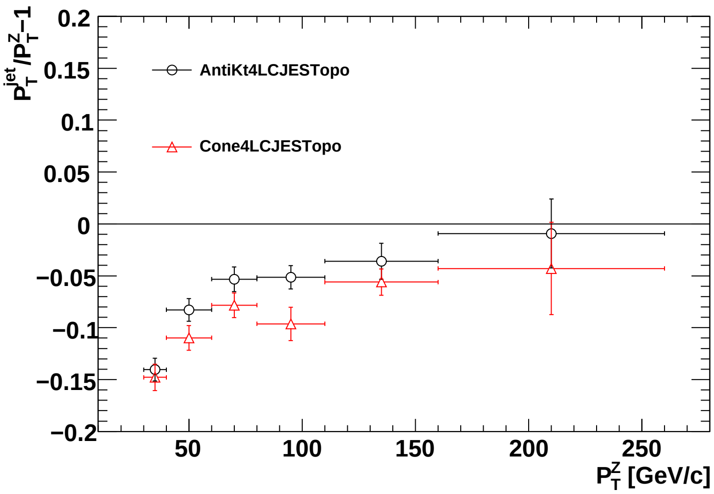

(a) $Z \rightarrow e^+e^-$

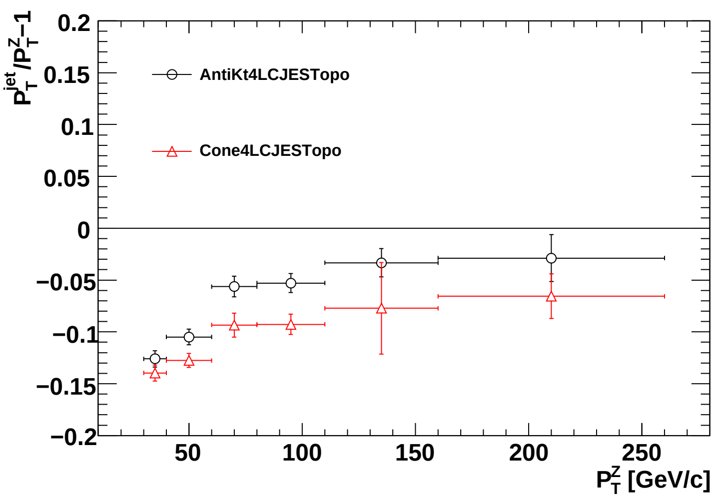

(b) $Z \rightarrow \mu^+\mu^-$

Figure 6–9: Comparison of p_T balance vs p_T^Z for narrow local hadronically calibrated cone and anti-k_T jets using topological clusters as input. Plots are for simulated $Z(\rightarrow e^+e^-)$ + Jet (a) and $Z(\rightarrow \mu^+\mu^-)$ + Jet (b) events.

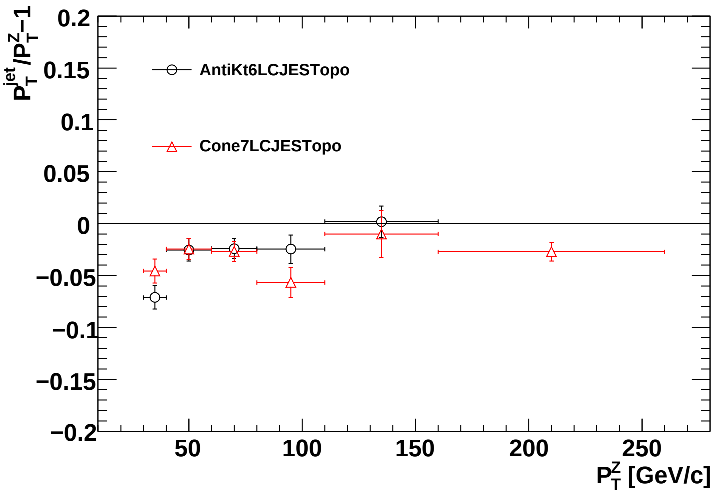

(a) $Z \to e^+e^-$

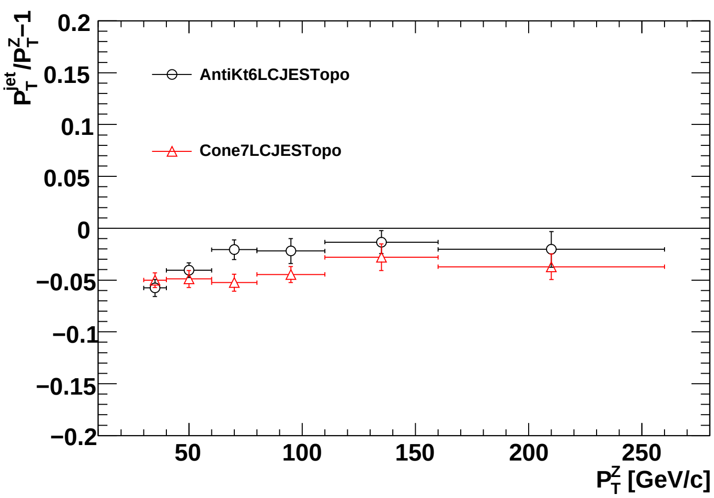

(b) $Z \to \mu^+\mu^-$

Figure 6–10: Comparison of p_T balance vs p_T^Z for wide local hadronically calibrated cone and anti-k_T jets using topological clusters as input. Plots are for simulated $Z(\to e^+e^-)$ + Jet (a) and $Z(\to \mu^+\mu^-)$ + Jet (b) events.

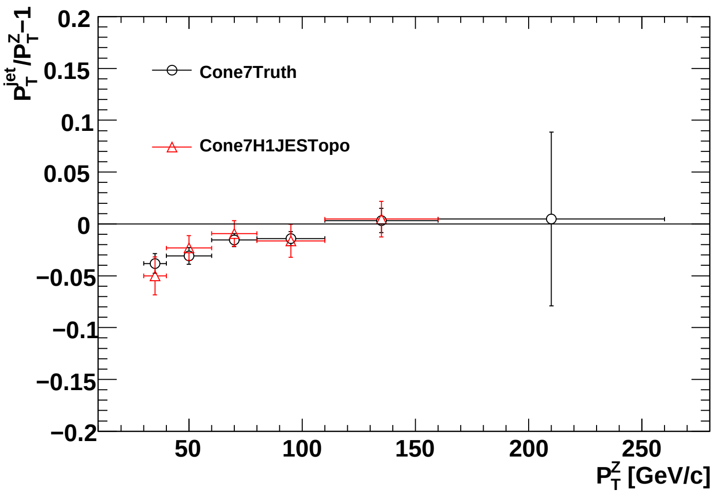

(a) $Z \to e^+e^-$

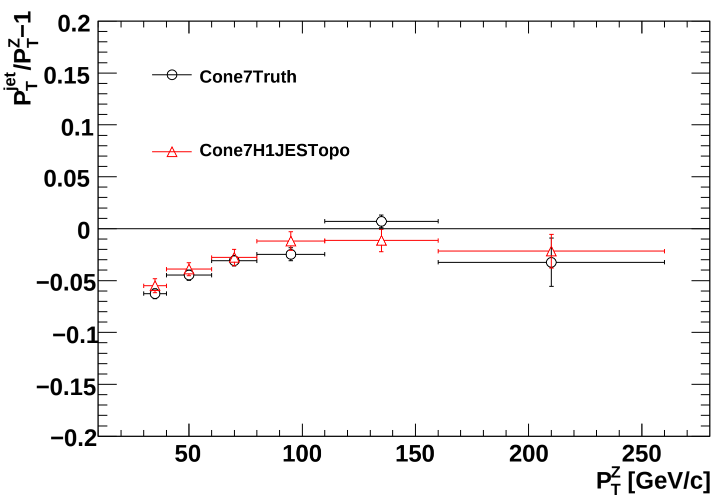

(b) $Z \to \mu^+\mu^-$

Figure 6–11: Plot of p_T balance vs p_T^Z for the "best" reconstructed $\Delta R = 0.7$ cone jet, using H1 calibrated topological clusters as input with global re-scaling, compared with truth jet. Plots are for simulated $Z(\to e^+e^-)$ + Jet (a) and $Z(\to \mu^+\mu^-)$ + Jet (b) events.

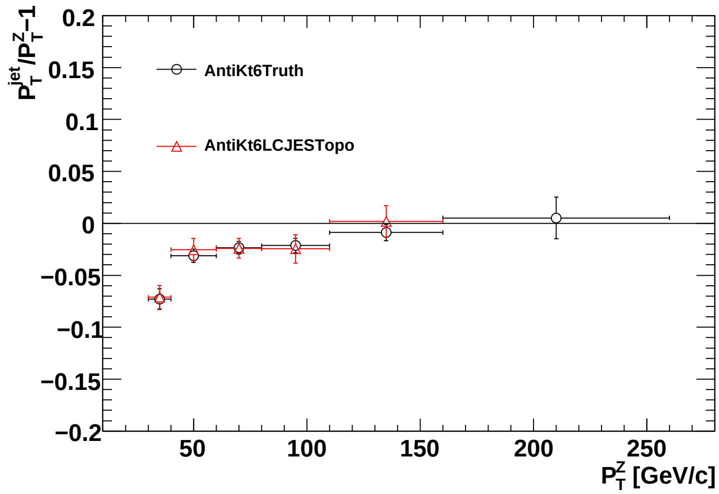

(a) $Z \to e^+e^-$

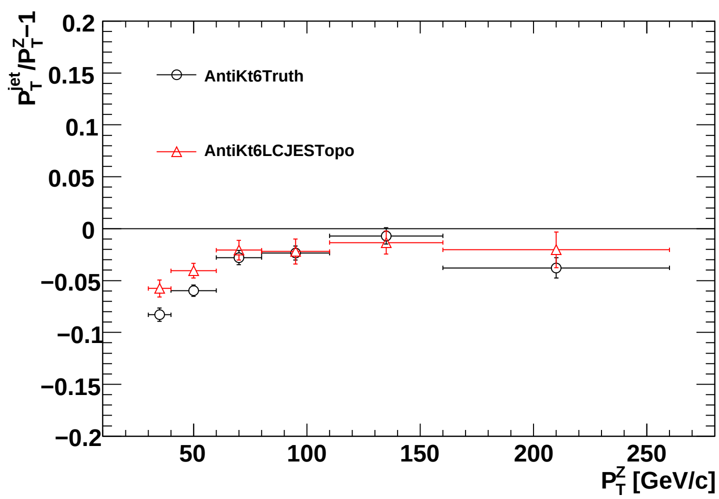

(b) $Z \to \mu^+\mu^-$

Figure 6–12: Plot of p_T balance vs p_T^Z for the "best" reconstructed $D = 0.6$ anti-k_T jet, using local hadronically calibrated topological clusters as input with global rescaling. Plots are for simulated $Z(\to e^+e^-)$ + Jet (a) and $Z(\to \mu^+\mu^-)$ + Jet (b) events.

CHAPTER 7
Conclusion

A precise measurement of the jet energy scale at ATLAS is required for many of the planned physics analyses to be successful. It is very important that the jet energy calibration at ATLAS be checked using data from real collisions *in situ*. In this thesis, the *in situ* technique of p_T balancing using $Z(\rightarrow e^+e^-)$ + Jet and $Z(\rightarrow \mu^+\mu^-)$ + Jet events was investigated as a possible candidate for testing the jet energy calibration performance. In the region where $p_T^Z > 60$ GeV/c, the technique has been shown to be a viable way of making a general test of the calibration of jets, to within 3%. At lower p_T, however, the technique begins to suffer from a kinematic bias, and becomes a less reliable indicator of jet calibration performance.

The effect of background processes on the p_T balance in Z + Jet events was shown to be negligible ($< 1\%$), and the systematic variations of p_T balance from altering the signal selection cuts was found to be less than 4%. In terms of the performance of reconstructed jets using p_T balancing in Z + Jet events, the anti-k_T algorithm was shown to be less sensitive to the choice of jet input and calibration scheme than the cone algorithm, with differences in p_T balance of less than 3%. The best performing combination of jet input and calibration with respect to truth jet for the $\Delta R = 0.7$ cone algorithm were topological clusters with H1 calibration and global re-scaling. For the $D = 0.6$ anti-k_T algorithm, the best performance was found with local hadronically calibrated topological clusters, with global re-scaling.

Due to the initial p_T of the interaction, the p_T balancing technique in Z + Jet events is affected by a kinematic bias which is most pronounced in the region where $p_T^Z < 60$ GeV/c. If this bias were well understood with an extensive monte carlo simulation study at parton level, it could potentially be corrected for and thus extend the useability of this technique to lower p_T. As well as study the performance of jets, once corrected it would also be possible to use p_T balancing in Z + Jet events to calibrate jets.

In future work, the technique should be applied to real ATLAS data. To make a statistical comparison with the results presented in this study (excluding Sections 5.3 and 5.6), 470 pb^{-1} of integrated luminosity would be required at a center of mass energy of 7 TeV. It is expected that after the first official physics run at the LHC, more than double this amount of integrated luminosity will be available (1 fb^{-1}). With this increase of statistics, it would be possible to make p_T balance measurements at larger energies ($p_T^Z > 260$ GeV/c). It is also recommended that the results in this study be compared with p_T balance studies using γ + Jet events.

References

[1] C. Amsler, M. Doser, M. Antonelli, D. Asner, K. Babu, H. Baer, H. Band, R. Barnett, E. Bergren, J. Beringer, *et al.*, “Review of particle physics,” *Physics Letters B*, vol. 667, no. 1-5, pp. 1–6, 2008.

[2] http://en.wikipedia.org/wiki/File:Elementary_particle_interactions.svg, 2008.

[3] *ATLAS Detector and Physics Performance Technical Design Report*, 1999. http://atlasinfo.cern.ch/Atlas/GROUPS/PHYSICS/TDR/access.html.

[4] O. Brüning, P. Collier, P. Lebrun, S. Myers, R. Ostojic, J. Poole, P. Proudlock, and C. Geneva, “LHC design report,” 2004.

[5] D. Perkins, *Introduction to high energy physics*. Cambridge Univ Press, 2000.

[6] E. Podgoršak, *Radiation physics for medical physicists*. Springer Verlag, 2005.

[7] B. Vachon, “Passage of particles through matter.” Slides from PHYS 620 lecture.

[8] M. Barbi, “Calorimetry.” Slides from Triumf Summer Institute 2007 lecture.

[9] F. Corriveau, “Calorimetry.” Slides from PHYS 620 lecture.

[10] D. Schouten, “Jet energy calibration in atlas,” Master’s thesis, Simon Fraser University, 2007.

[11] T. A. Collaboration, “Expected performance of the atlas experiment: detector, trigger and physics,” Tech. Rep. arXiv:0901.0512. CERN-OPEN-2008-020, Geneva, 2009.

[12] V. Barger and R. Phillips, *Collider physics*. Addison-Wesley, 1987.

[13] G. Blazey, J. Dittmann, S. Ellis, V. Elvira, K. Frame, S. Grinstein, R. Hirosky, R. Piegaia, H. Schellman, R. Snihur, *et al.*, “Run II jet physics,” *Arxiv preprint hep-ex/0005012*, 2000.

[14] M. Cacciari, G. P. Salam, and G. Soyez, “The anti-kt jet clustering algorithm,” *Journal of High Energy Physics*, vol. 2008, no. 04, p. 063, 2008.

[15] D. Lopez Mateos and F. E. Paige, “Inputs to jet reconstruction and calibration with the atlas detector using proton-proton collisions at $\sqrt{s} = 900$ gev,” Tech. Rep. ATL-COM-PHYS-2010-144, CERN, Geneva, Mar 2010.

[16] S. Resconi, “Jet and etmiss commissioning in atlas,” Nov 2009.

[17] I. Abt, T. Ahmed, S. Aid, V. Andreev, B. Andrieu, R. Appuhn, C. Arnault, M. Arpagaus, A. Babaev, H. Bärwolff, *et al.*, “The H1 detector at HERA,” *Nuclear Instruments and Methods in Physics Research A*, vol. 386, pp. 310–347, 1997.

[18] T. Barillari, E. Bergeaas Kuutmann, T. Carli, J. Erdmann, P. Giovannini, K. J. Grahn, C. Issever, A. Jantsch, A. Kiryunin, K. Lohwasser, A. Maslennikov, S. Menke, H. Oberlack, G. Pospelov, E. Rauter, P. Schacht, F. Span, P. Speckmayer, P. Stavina, and P. Strzenec, “Local hadronic calibration,” Tech. Rep. ATL-LARG-PUB-2009-001. ATL-COM-LARG-2008-006, CERN, Geneva, Jun 2008.

[19] S. Agostinelli, J. Allison, K. Amako, J. Apostolakis, H. Araujo, P. Arce, M. Asai, D. Axen, S. Banerjee, G. Barrand, *et al.*, “Geant4-a simulation toolkit,” *Nuclear Instruments and Methods in Physics Research-Section A Only*, vol. 506, no. 3, pp. 250–303, 2003.

[20] D. Lopez Mateos, E. W. Hughes, and A. Schwartzman, “A simple p_t- and η-dependent monte carlo-based jet calibration,” Tech. Rep. ATL-COM-PHYS-2009-076, CERN, Geneva, Feb 2009.

[21] A. Bhatti, F. Canelli, B. Heinemann, J. Adelman, D. Ambrose, J. Arguin, A. Barbaro-Galtieri, H. Budd, Y. Chung, K. Chung, *et al.*, “Determination of the jet energy scale at the Collider Detector at Fermilab,” *Nuclear Inst. and Methods in Physics Research, A*, vol. 566, no. 2, pp. 375–412, 2006.

[22] J. Campbell, J. Huston, and W. Stirling, “Hard interactions of quarks and gluons: a primer for LHC physics,” *Reports on Progress in Physics*, vol. 70, no. 1, pp. 89–194, 2007.

[23] M. Hurwitz, “Understanding the jet energy scale using photon-jet balancing.” ATLAS Internal Note, February 2009.

[24] G. Choudalakis, E. Feng, A. Messina, and L. Pribyl, "In situ jet energy scale calibration using direct photon+jet balance," Tech. Rep. ATL-PHYS-INT-2010-023. ATL-COM-PHYS-2009-644, CERN, Geneva, Feb 2010.

[25] L. Apanasevich, C. Balazs, C. Bromberg, J. Huston, A. Maul, W. Tung, S. Kuhlmann, J. Owens, M. Begel, T. Ferbel, *et al.*, "k_T effects in direct-photon production," *Physical Review D*, vol. 59, no. 7, p. 74007, 1999.

[26] T. Sjöstrand, S. Mrenna, and P. Skands, "PYTHIA 6.4 physics and manual," *Journal of High Energy Physics*, vol. 2006, p. 026, 2006.

[27] M. Mangano, F. Piccinini, A. Polosa, M. Moretti, and R. Pittau, "ALPGEN, a generator for hard multiparton processes in hadronic collisions," *Journal of High Energy Physics*, vol. 2003, p. 001, 2003.

[28] G. Corcella, I. Knowles, G. Marchesini, S. Moretti, K. Odagiri, P. Richardson, M. Seymour, and B. Webber, "HERWIG 6: An event generator for hadron emission reactions with interfering gluons (including supersymmetric processes)," *Journal of High Energy Physics*, vol. 2001, p. 010, 2001.

[29] J. Butterworth, J. Forshaw, and M. Seymour, "Multiparton interactions in photoproduction at HERA," *Zeitschrift für Physik C Particles and Fields*, vol. 72, no. 4, pp. 637–646, 1996.

[30] M. Mangano, M. Moretti, and R. Pittau, "Multijet matrix elements and shower evolution in hadronic collisions:-jets as a case study* 1," *Nuclear Physics B*, vol. 632, no. 1-3, pp. 343–362, 2002.

[31] B. P. Kersevan and E. Richter-Was, "The monte carlo event generator acermc version 1.0 with interfaces to pythia 6.2 and herwig 6.3," *Computer Physics Communications*, vol. 149, no. 3, pp. 142 – 194, 2003.

[32] S. Chekanov, "Understanding the jet energy scale using p_t balance for z+jet events." ATLAS Internal Note, March 2009.

[33] E. S. i Solé, *Simulation of the Measurement of the Inclusive Jet Cross Sections in Z($\rightarrow e^+e^-/\rightarrow \mu^+\mu^-$)+jets Events in pp Collisions at 14 TeV with the ATLAS experiment*. PhD thesis, Universitat Autònoma de Barcelona, 2009.

[34] T. C. Collaboration, "Calibration of the absolute jet energy scale with $z(\rightarrow \mu^+\mu^-)$ + jet events at CMS," Jul 2009.